Available online at www.sciencedirect.com

SCIENCE DIRECT®

Remote Sensing of Environment 97 (2005) 137 – 162

Remote Sensing of Environment

www.elsevier.com/locate/rse

Prototyping a global algorithm for systematic fire-affected area mapping using MODIS time series data

D.P. Roy[a,*], Y. Jin[b], P.E. Lewis[c], C.O. Justice[b]

[a]*Department of Geography, 1113 LeFrak Hall, University of Maryland, College Park, MD 20742 and NASA Goddard Space Flight Center, Code 614.5, USA*
[b]*Department of Geography, 1113 LeFrak Hall, University of Maryland, College Park, MD 20742, USA*
[c]*Remote Sensing Unit and NERC Centre for Terrestrial Carbon Dynamics, Department of Geography, University College London, 26 Bedford Way, London, WC1H 0AP, UK*

Received 5 October 2004; received in revised form 30 March 2005; accepted 2 April 2005

Abstract

The remote sensing of Earth surface changes is an active research field aimed at the development of methods and data products needed by scientists, resource managers, and policymakers. Fire is a major cause of surface change and occurs in most vegetation zones across the world. The identification and delineation of fire-affected areas, also known as burned areas or fire scars, may be considered a change detection problem. Remote sensing algorithms developed to map fire-affected areas are difficult to implement reliably over large areas because of variations in both the surface state and those imposed by the sensing system. The availability of robustly calibrated, atmospherically corrected, cloud-screened, geolocated data provided by the latest generation of moderate resolution remote sensing systems allows for major advances in satellite mapping of fire-affected area. This paper describes an algorithm developed to map fire-affected areas at a global scale using Moderate Resolution Imaging Spectroradiometer (MODIS) surface reflectance time series data. The algorithm is developed from the recently published Bi-Directional Reflectance Model-Based Expectation change detection approach and maps at 500 m the location and approximate day of burning. Improvements made to the algorithm for systematic global implementation are presented and the algorithm performance is demonstrated for southern African, Australian, South American, and Boreal fire regimes. The algorithm does not use training data but rather applies a wavelength independent threshold and spectral constraints defined by the noise characteristics of the reflectance data and knowledge of the spectral behavior of burned vegetation and spectrally confusing changes that are not associated with burning. Temporal constraints are applied capitalizing on the spectral persistence of fire-affected areas. Differences between mapped fire-affected areas and cumulative MODIS active fire detections are illustrated and discussed for each fire regime. The results reveal a coherent spatio-temporal mapping of fire-affected area and indicate that the algorithm shows potential for global application.

Keywords: Fire; Fire-affected area; Burned area; Change detection; BRDF; MODIS; Time series

1. Introduction

Fire is a prominent disturbance factor and is an agent of environmental change with local to regional impacts on land use, productivity, carrying capacity, and biodiversity, and regional to global impacts on hydrologic, biogeochemical, and atmospheric processes (Csiszar et al., 2004). Fire plays a role in a number of land surface atmosphere interactions and is a significant source of trace gases and aerosols impacting atmospheric chemistry and the radiation budget (Crutzen & Andreae, 1990; French et al., 2003; Govaerts et al., 2002; Scholes & Andreae, 2000; van der Werf et al., 2003). Fire is an important ecosystem process effecting vegetation structure and composition (Johnson & Miyanishi, 1997) and in many land use systems is a

* Corresponding author.
E-mail address: droy@kratmos.gsfc.nasa.gov (D.P. Roy).

0034-4257/$ - see front matter © 2005 Elsevier Inc. All rights reserved.
doi:10.1016/j.rse.2005.04.007

proximate cause or indicator of land cover change (Bucini & Lambin, 2002; Cochrane, 2003; Janetos & Justice, 2000). The frequency, intensity, season, and type of fire that prevails in an area are collectively referred to as the fire regime. It remains unclear if fire regimes will change as human population, their land use practices, and the climate change (Stocks, 1998; Murphy et al., 1999; UNEP, 2002). Certainly, there is a perceived increasing incidence, extent, and severity of uncontrolled burning globally that has lead to calls for international environmental policy concerning fire (Stocks et al., 2001). Such concerns strengthen the need to provide reliable fire information to policymakers, scientists, and resource managers. The satellite derived information, includes the location, timing, instantaneous radiative power, temperature and size of active fires, and the spatial extent of burning. In this paper, we use the term "fire-affected area" to denote the area subjected to fire. This is in recognition that fire often does not burn the entire surface it passes over and because more pejorative terms, such as "fire scar" or "burn scar", do not reflect the beneficial ecological effects of fire in many parts of the world.

Satellite remote sensing provides the only means of monitoring vegetation burning at regional to global scale. The Vegetation Fire Information System proposed at the Dahlem Conference on Fire in the Environment in 1992 provided a vision for an information system composed of satellite and in-situ observations to serve the global change community (Crutzen & Goldammer, 1993). Subsequently, remote sensing requirements for measuring the timing and spatial extent of fires globally have been included in summary documents generated by the Committee on Earth Observation Satellites (CEOS) and the Global Climate Observing System (GCOS) (CEOS, 2000; GCOS, 1997). Satellite data have been used to monitor fire globally for more than two decades using active fire detection algorithms developed for different sensors to take advantage of the elevated radiance signal of hot fires (Arino & Rosaz, 1999; Dozier, 1981; Elvidge et al., 2001; Giglio et al., 2003; Matson & Dozier, 1981; Prins & Menzel, 1992). It is well established that for most fire regimes satellite active fire detections do not reliably define the fire-affected area. This is because the satellite may not overpass sufficiently frequently to capture the spatial details of how fires propagate across landscapes, and because clouds and optically thick smoke may preclude active fire detection (Justice et al., 2002b; Robinson, 1991). Recognizing these limitations, methods to map fire-affected area have been developed in the last decade using moderate and coarse spatial resolution satellite data (e.g., Barbosa et al., 1999; Eva & Lambin, 1998a; Fredericksen et al., 1990; Fraser et al., 2000; Kasischke & French, 1995; Roy et al., 2002b; Simon et al., 2004; Tansey et al., 2004; Zhang et al., 2003). Most approaches capitalize on the spectral impact of fire effects (associated with deposition of charcoal and ash, removal of vegetation, and alteration of the vegetation structure) and use multi-temporal satellite data, which provide several advantages over single date data for mapping fire-affected areas (Eva & Lambin, 1998b; Pereira et al., 1997). Despite the range of studies undertaken, there is no consensus algorithm and no global algorithm has yet been implemented on more than 1 year of remotely sensed data (Simon et al., 2004; Grégoire et al., 2003). Comparison of fire-affected area products generated recently using contemporaneous time series data sensed by the Moderate Resolution Imaging Spectroradiometer (MODIS) (Roy, 2003), the Systeme Pour l'Observation de la Terre (SPOT-VEGETATION) (Tansey et al., 2004), and the Along Track Scanning Radiometer (ATSR-2) (Simon et al., 2004) for southern Africa indicate substantive differences and highlight the need for rigorous product validation (Korontzi et al., 2004).

The availability of robustly calibrated, atmospherically corrected, cloud-screened, geolocated data provided by the latest generation of moderate resolution remote sensing systems allows for major advances in satellite mapping of fire-affected area. Arguably, these data allow for the development of more physically based algorithms that are less dependent upon imprecise but noise tolerant classification techniques. As part of NASA's Earth Observing System (EOS), the Moderate Resolution Imaging Spectroradiometer (MODIS) is onboard the Terra (launched 1999) and Aqua (launched 2001) polar orbiting satellites and their data are being used to generate global coverage data products on a systematic basis (Justice et al., 2002a). The algorithm used to define the MODIS active fire product has been refined several times (Giglio et al., 2003; Justice et al., 2002a; Kaufman et al., 1998). A complementary MODIS algorithm defined to map fire-affected area has been developed and demonstrated in southern Africa (Roy, 2003; Roy et al., 2002b). The algorithm uses a bi-directional reflectance model-based change detection approach to map the 500 m location and approximate day of burning. It detects the approximate date of burning by locating the occurrence of rapid changes in daily MODIS reflectance time series. The algorithm maps the spatial extent of recent fires and not of fires that occurred in previous seasons or years. The algorithm is an improvement on previous methods due to the use of a bi-directional reflectance model to deal with angular variations found in satellite data and the use of a statistical measure to detect change probability from a previously observed state. The algorithm does not use training data and is adaptive to the number, viewing, and illumination geometry of the data, and to the amount of noise in the data. This paper describes refinements and improvements made to the algorithm for its systematic global application and illustrates its functioning for southern African, Australian, South American, and Boreal fire regimes. The improved algorithm will be implemented in the MODIS land production system in an attempt to systematically map

fire-affected areas globally for the 6+-year MODIS observation record.

2. Data

The MODIS fire-affected area product is generated from time series of daily 500 m MODIS land surface reflectance data derived in the manner described below. Measurements in the seven MODIS land surface reflectance bands (Table 1) are corrected for atmospheric effects, including aerosols (Vermote et al., 2002). These data and associated quality assessment information are gridded into a Level 2G format that stores the MODIS observations sensed over a 12-h period (Wolfe et al., 1998). The Level 2G product is defined in the MODIS land product equal area sinusoidal projection in geolocated tiles. Each tile has fixed earth-locations covering an area of approximately 1200×1200 km ($10° \times 10°$ at the equator). Globally, there are 460 non-overlapping tiles, of which 326 contain land pixels. The L2G data are processed into daily intermediate files where all high view zenith (>65°), high solar zenith (>65°), bad quality, high aerosol, snow, cloudy, and non-land, MODIS observations labeled in the Level 2G land surface reflectance product are rejected. These data provide good quality observations of the land surface, although shadow contaminated observations and a minority of cloud, snow, and water observations may remain. When more than one MODIS observation is sensed over a given pixel per day, occurring at high MODIS view zenith angles and at latitudes greater than approximately 30°, the observation that has the greatest ratio of observation to pixel gridcell area is retained with the associated viewing and solar angles (Wolfe et al., 1998). This gives a maximum of one observation per geolocated pixel per day. In this paper, all results are shown using the most recently processed Collection 4 MODIS Terra satellite data only. The MODIS 1 km night and day time active fire product, which locates 1 km MODIS pixels containing certain actively burning fires at the time of satellite overpass (Giglio et al., 2003), is used to verify the algorithm.

Table 1
Summary of the MODIS 500 m land surface reflectance bands and conservative land surface reflectance one standard deviation (σ_λ) noise estimates (Vermote et al., 2002; Vermote, personal communication)

MODIS band	Central wavelength (μm)	σ_λ (reflectance scaled 0–1)
1	0.645	0.004
2[a]	0.858	0.015
3	0.469	0.003
4	0.555	0.004
5[a]	1.240	0.013
6[a]	1.640	0.010
7[a]	2.130	0.006

[a] Denotes MODIS bands used by the global fire-affected area mapping algorithm.

3. Study regions

The MODIS algorithm to map global fire-affected area was refined by prototyping focused on study regions in southern Africa, Australia, South America, and the Russian Federation. These four study regions were chosen to encompass tropical, sub-tropical, boreal, temperate, and arid environments. They are also located where there are networks of fire researchers, including those supporting the Global Observations of Forest Cover/Global Observation of Landcover Dynamics (GOFC/GOLD)-Fire initiative (Justice et al., 2003), who are available to assess and help validate the MODIS fire products. Importantly, the study regions capture a range of the major factors that influence the accuracy of fire-affected area products derived from satellite data. These factors include the spatial characteristics of fire-affected areas, the degree of spectral change from unburned to burned vegetation, and spectral changes of a similar direction and magnitude that are not caused by burning (Eva & Lambin, 1998b; Roy et al., 2002b, in press). The study regions cover 29 MODIS tiles and account for approximately 9% of the global land surface.

3.1. Southern Africa

The region encompassed by the Southern Africa Fires and Atmospheric Research Initiative (SAFARI 2000) (Swap et al., 2002) was selected as the first regional test of the MODIS fire-affected area product. This region includes all of sub-equatorial Africa, including Madagascar, and comprises 15 MODIS tiles (Fig. 1). The largest portion of southern Africa has a climate that is characterized by a single rainy season and a long dry season. This rainfall seasonality provides a fire-prone climate and the savannas of Africa are thought to experience the most extensive biomass burning in the world (Cahoon et al., 1992; Scholes & Andreae, 2000). Most fires occur in the dry season, from approximately May to October, when herbaceous vegetation is either dead (annual grasslands) or dormant, and when deciduous trees have shed their leaves, thereby contributing to an accumulation of dry and fine fuels that are easily combustible (Frost, 1999). Fire is integral to many agricultural practices and is an important land management tool. The majority of fires are thought to be anthropogenic, with non-anthropogenic lightning ignited fires associated with early wet-season thunderstorms (Frost, 1999). A prototype southern Africa fire-affected area product was created (Roy, 2003) using the algorithm described by Roy et al. (2002b). This prototype was used in support of SAFARI 2000 to model trace gasses and emissions (Korontzi et al., 2004) and has subsequently been refined using the algorithm described in this paper.

3.2. Australia

Like southern Africa, much of Australia has a fire-prone climate. The Australian study region comprises 7 MODIS

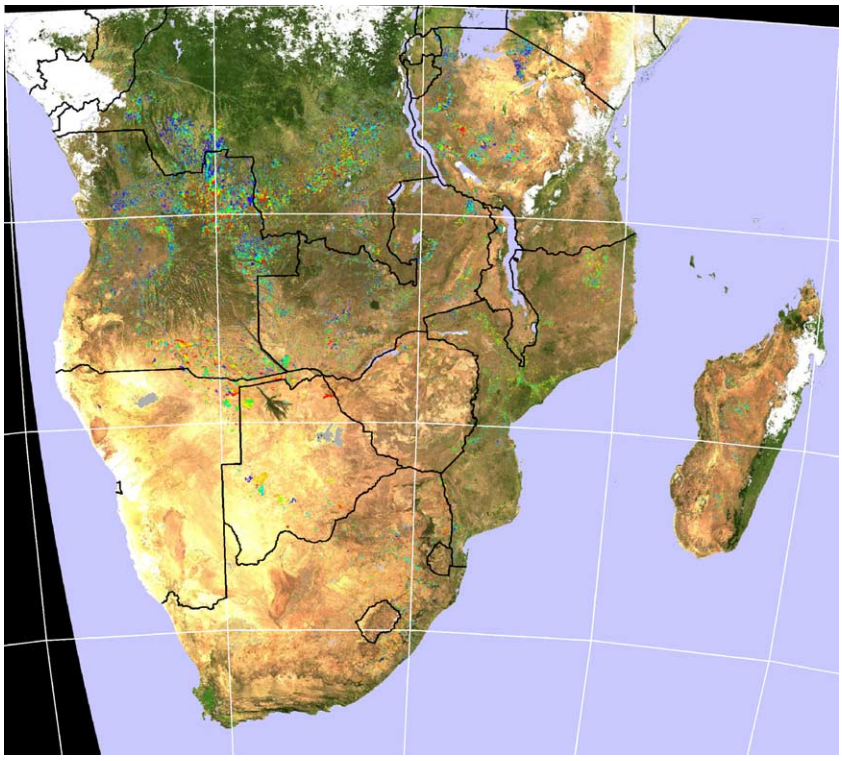

Fig. 1. Southern Africa study region and example MODIS fire-affected areas. Country borders (black lines) and 10° meridians (from 10° to 50° East) and parallels (from 0° to 30° South) are shown (white lines). MODIS 500 m fire-affected areas mapped for 1.5 months are illustrated with a rainbow color scale to denote the approximate day of burning from June 23rd (violet) to August 8th (red), 2002. Extensive burning is evident in much of Angola and the southern parts of the Democratic Republic of the Congo. Areas not mapped due to persistent cloud are shown white. The fire-affected areas are shown superimposed on 500 m MODIS nadir bi-directional modeled red (0.645 μm), green (0.555 μm), and blue (0.469 μm) reflectance to provide geographic context. Water bodies are colored lilac. The black areas denote adjacent MODIS tiles not included in this 15-tile study region. See Fig. 13 for an enlarged view of a 450 × 250 km subset.

tiles (Fig. 2) that encompass more than two thirds of Australia, including tropical parts in the Northern Territory and northern western Australia, and more arid and temperate regions in the centre and to the south of western Australia, south Australian, and New South Wales. The fire season in the tropical savannas is determined by the annual arrival and departure of the monsoon (Tapper et al., 1993). Fire is extensive and frequent in Australia's savannas, occurring from approximately March to December (Williams et al., 2002). Recent continental-scale fire mapping using NOAA-AVHRR satellite data for 1997 to 2001 has shown that the greatest extent of fire occurs in the tropical savanna of northern Australia, and of this region an average of 19% burned annually (Russell-Smith et al., 2003). Spinifex grasslands cover more than 25% of the Australia landscape and grassland fires can be extensive, frequently exceeding many thousands of square kilometers (Bradstock et al., 2002). In semi-arid and arid Australia, fire occurrence is strongly dependent on herbaceous plants that become dominant after irregular high-rainfall periods. Fires are lit naturally by lightning, especially in the late dry season, and the use of fire by aboriginal peoples mainly for pastoral purposes is also extensive in northern Australia (Dyer et al., 2001; Russell-Smith et al., 2003). Accidental fires and arson fires are frequently reported in the media.

3.3. South America

The South America study region comprises 3 MODIS tiles in the humid tropics (Fig. 3) including parts of Brazil (Amazonas, Para, Mato Grosso), most of Bolivia, parts of Peru and Chile to the West, and the northern tip of Paraguay. Fires in this region are largely anthropogenic and are typically associated with clearing of new land and maintenance of previously cleared lands (Cardoso et al., 2003; de Miranda & John, 2000). Fires predominate in the dry season when lower moisture conditions facilitate the use of fires for land management (Setzer et al., 1992). The grassland/savanna cerrado is considerably more flammable than the intact tropical evergreen forests. In extremely dry years, uncontrolled fires caused by current land use practices have become a concern due to the potentially vast area of tropical evergreen forest affected (Setzer & Pereira, 1991), with a positive feedback postulated wherein successive fires become more intense and more susceptible to fires originating from nearby pasturelands and agricultural fields (Cochrane et al., 1999).

3.4. Russian Federation

The study region comprises 4 MODIS tiles (Fig. 4A and B) that encompass boreal forests to the north and south of

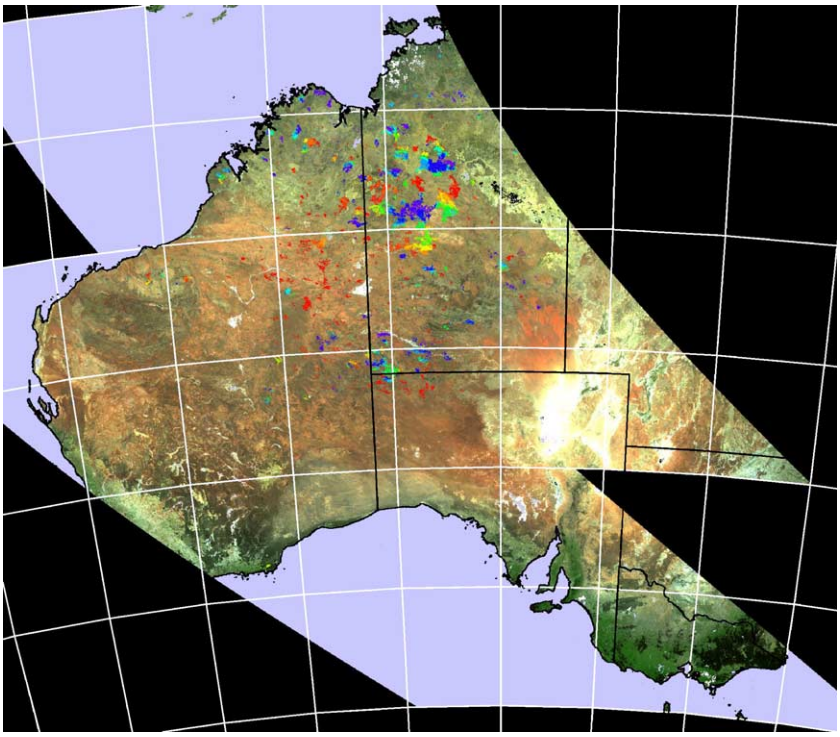

Fig. 2. Australia study region and example MODIS fire-affected areas. State borders (black lines) and 5° meridians (from 115° to 150° East) and parallels (from 10° to 40° South) are shown (white lines). MODIS 500 m fire-affected areas mapped for 1 month are illustrated with a rainbow color scale to denote the approximate day of burning from October 1st (violet) to October 31st (red), 2002. Extensive burning is evident in the Northern Territory and the NE of western Australia. The fire-affected areas are shown superimposed on 500 m MODIS nadir bi-directional modeled red (0.645 μm), green (0.555 μm), and blue (0.469 μm) reflectance. Water bodies are colored lilac. The black areas denote adjacent MODIS tiles not included in this 7-tile study region. See Fig. 14 for an enlarged view of a 450 × 250 km subset.

the Arctic Circle and East of the Ural Mountains. Tree growth is limited by permafrost and a very short growing season (Stocks et al., 1996). Fire impacts large areas of boreal forest, where evidence of past fire history is dominant in the vegetation patterns (Goldammer & Furyaev, 1996; Shvidenko & Nilsson, 2000). The fire season in southern Siberia begins in spring from early May, moves northward as spring arrives at higher latitudes, and peaks in the dry summer (Korovin, 1996). Approximately 70% of the fires in the Russia Federation are thought to occur in light coniferous pine and larch-dominated stands, and only about 15% in dark coniferous boreal forest (Korovin, 1996). Surface fires are typical, but patchy crown fires are common and may dominate in severe fire seasons to cause near total tree mortality (Furyaev, 1996; Korovin, 1996). A large percentage of fires are caused by human activities but where population densities are low they are caused by lightning (Korovin, 1996).

4. Original bi-directional reflectance model-based change detection algorithm

Our goal is to develop a global algorithm to continuously map recently occurring fire-affected areas on a systematic and automated basis from MODIS observations. A number of substantive improvements have been made to the bi-directional reflectance model-based change detection algorithm described by Roy et al. (2002b). We overview this original algorithm below and describe algorithm improvements in subsequent sections. We refer to the improved algorithm as the global algorithm.

Most land surfaces are strongly anisotropic reflectors at reflective wavelengths (Barnsley et al., 1997; Kimes, 1983; Pinty & Verstraete, 1992). This anisotropy, combined with the angular sensing and illumination variations present in wide field-of-view satellite time series data, introduce bi-directional reflectance variations that complicate the identification of surface change. The majority of coarse/moderate spatial resolution algorithms developed to map fire-affected areas use spectral indices. Spectral indices have attractive properties, such as reducing certain shadow, illumination, and topographic induced variations (Holben & Justice, 1981), but can still have significant directional effects (Gao et al., 2002; Meyer et al., 1995). For example, Leroy and Hautecoeur (1999) found daily spectral index variations of the order 0.05–0.2 due to directional effects in POLarization and Directionality of the Earth's Reflectances instrument (POLDER) data over the African continent. Failure to account for these effects implies a commensurate reduction in change detection capabilities. Regardless of directional effects, simple modeling work has demonstrated

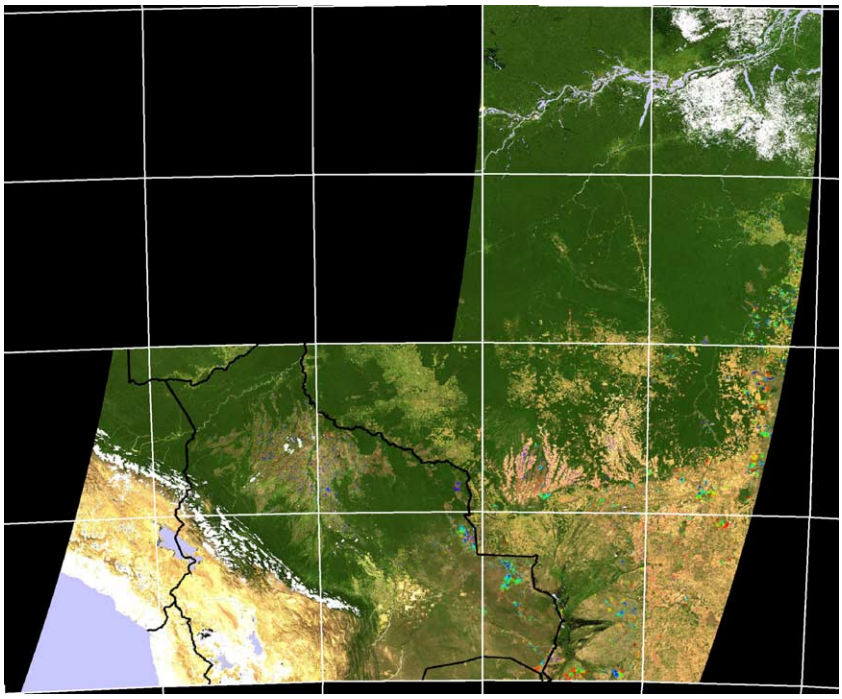

Fig. 3. South America study region (parts of Brazil, Bolivia, Peru, Chile, and Paraguay) and example MODIS fire-affected areas. Country borders (black lines) and 5° meridians (from 70°, 65°, 60°, 55° to 50° West) and parallels (from 0° to 20° South) are shown (white lines). MODIS 500 m fire-affected areas mapped for 1 month are illustrated with a rainbow color scale to denote the approximate day of burning from August 1st (violet) to August 31st (red), 2002. Extensive burning is evident in NE Bolivia and SW and eastern parts of Brazil. Areas not mapped due to persistent cloud are shown in white. The fire-affected areas are shown superimposed on 500 m MODIS nadir bi-directional modeled red (0.645 μm), green (0.555 μm), and blue (0.469 μm) reflectance. Water bodies are colored lilac. The black areas denote adjacent MODIS tiles not included in this 3-tile study region. See Fig. 15 for enlarged views of two 250 × 250 km subsets.

that ratio spectral indices may be sensitive in a non-linear manner to the size and combustion completeness of the fire and so may provide variable detection capabilities when used to map fire-affected areas (Roy & Landmann, in press). Composited satellite data are used to reduce the impact of atmospheric contamination and directional effects (Holben, 1986) and are used by the majority of algorithms developed to map fire-affected areas from coarse and moderate spatial resolution satellite data. Directional reflectance effects remain in composited data but restricting observations to close-to-nadir to minimize their impact reduces the effective temporal sampling frequency and discards the potentially useful information found in off-nadir observations (Cihlar et al., 1994).

The bi-directional reflectance model-based change detection algorithm is a generic change detection method that is applied independently to geolocated pixels over a long time series (weeks to months) of reflectance observations (Roy et al., 2002b). Reflectances sensed within a temporal window of a fixed number of days are used to predict the reflectance on a subsequent day. A statistical measure is used to determine if the difference between the predicted and observed reflectance is a significant change of interest. Rather than attempting to minimize the directional information present in wide field-of-view satellite data by compositing, or by the use of spectral indices, these information are used to model the directional dependence of reflectance. This provides a semi-physically based method to predict change in reflectance from the previous state.

The directional dependence of reflectance varies as a function of the sun-target-sensor geometry and is described by the Bi-directional Reflectance Distribution Function (BRDF) (units of sr^{-1}). Methods have been developed to model the BRDF with a limited number of parameters and then to estimate the model parameters from a finite set of remotely sensed observations (Lucht, 2004). The semi-empirical RossThick-LiSparse reciprocal BRDF model is used as it performs robustly in the global MODIS BRDF/albedo product (Schaaf et al., 2002). Like other linear kernel-driven models, it allows analytical model inversion with an estimate of uncertainty in the model parameters and linear combinations thereof (Lucht & Lewis, 2000; Lucht & Roujean, 2000). It also implicitly models surface heterogeneity (assuming linear scaling of reflectance). Other BRDF models may be used but we note that the RossThick-LiSparse reciprocal model satisfies the general algorithm requirement to predict reflectance under similar MODIS sensing and illumination geometries (Roy et al., 2002b). At each geolocated pixel, the three parameter RossThick-LiSparse reciprocal BRDF model is inverted against $m \geq 7$ reflectance observations sensed in a temporal window of $n = 16$ days duration. These values are the same as those used to compute the MODIS 16-day BRDF/albedo product (Schaaf et al., 2002). A minimum of 7 observations

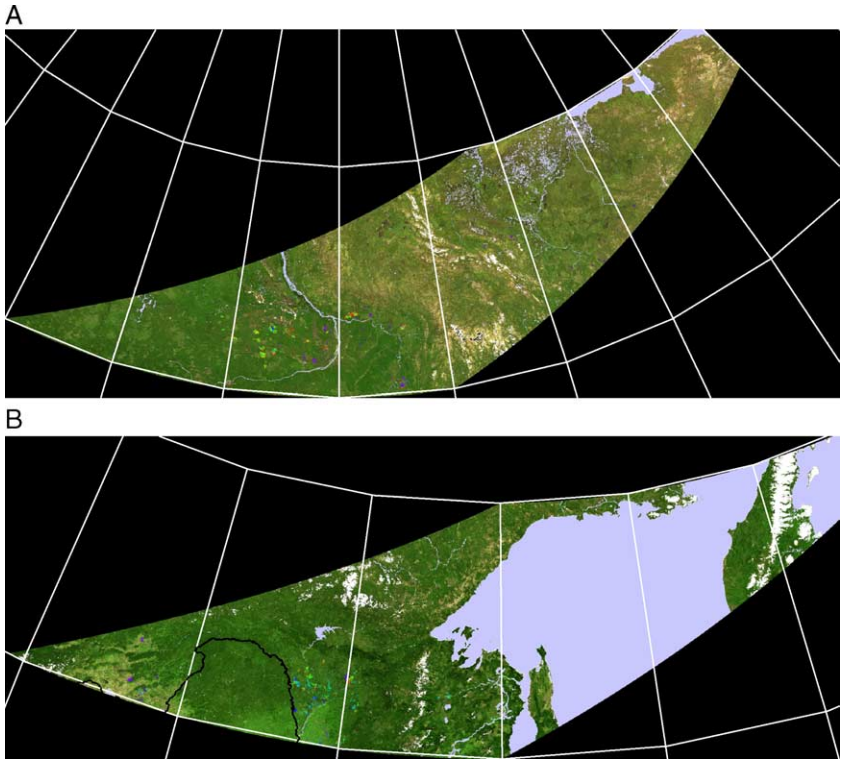

Fig. 4. (A) Russian Federation study region encompassing the Arctic Circle (Central Siberian Plateau in the West, Anadyr in the East). 10° meridians (from 90° to 180° East) and parallels (60° and 70° North) are shown (white lines). The Lena River is evident running approximately North–South between longitudes 120° and 130° East. MODIS 500 m fire-affected areas mapped for 1 month are illustrated with a rainbow color scale to denote the approximate day of burning from July 1st (violet) to July 31st (red), 2002. Extensive burning is evident to the West of the Lena River, near Yakutsk. The fire-affected areas are shown superimposed on 500 m MODIS nadir bi-directional modeled red (0.645 μm), green (0.555 μm), and blue (0.469 μm) reflectance. Water bodies are colored lilac. The black areas denote adjacent MODIS tiles not included in this 2-tile study region. See Fig. 16 for an enlarged view of a 450 × 250 km subset. (B) Russian Federation study region (Kamchatka Peninsular in the East) including parts of NE China. Country borders (black lines) and 10° meridians (from 110° to 160° East) and parallels (from 50° and 60° North) are shown (white lines). MODIS 500 m fire-affected areas mapped for 1 month are illustrated with a rainbow color scale to denote the approximate day of burning from May 1st (violet) to May 31st (red), 2002. Extensive burning is evident to the East of the Chinese border. Water bodies are colored lilac. The black areas denote adjacent MODIS tiles not included in this 2-tile study region.

is used as this provides more than twice as many observations as there are RossThick-LiSparse BRDF model parameters and MODIS studies indicate that using fewer observations provide unstable results (Gao et al., 2001). The BRDF model parameters are used to compute predicted reflectance and uncertainties for the viewing and illumination angles of a subsequent observation. A Z-score is used as a normalized measure related to the probability of the new observation belonging to the same set as that used in the model inversion:

$$Z_\lambda = \frac{\rho_{\text{new}}(\lambda, \Omega, \Omega') - \rho(\lambda, \Omega, \Omega')}{\varepsilon} \quad (1)$$

$$\varepsilon = e\sqrt{\frac{1}{w}}$$

where Z_λ is the Z-score value, $\rho_{\text{new}}(\lambda, \Omega, \Omega')$ is the new reflectance observation, $\rho(\lambda, \Omega, \Omega')$ is the model predicted reflectance at wavelength λ computed by analytical inversion of the BRDF model against m previous reflectance observations, Ω and Ω' are the viewing and illumination vectors respectively of the new reflectance observation, and ε is the model prediction error defined by the product of e, the root mean squared of the residuals of the BRDF inversion (used as an estimate of noise in the observations and the lack of ability of the model to fit the measurements), and w is the 'weight of determination' of $\rho_{\text{new}}(\lambda, \Omega, \Omega')$ (Lucht & Lewis, 2000). Z_λ is adaptive to the viewing and illumination angles of the new observation, as well as the angular distribution, amount of noise, and number of the observations used in the BRDF inversion (Roy et al., 2002b).

The computation (1) is repeated, moving through the reflectance time series in daily steps to detect change. This is analogous to compositing the reflectance time series with overlapping consecutive compositing periods to ensure that change events that occur between periods are captured (Roy et al., 1999). Rather than using training data, thresholds defined by the noise characteristics of the reflectance data and knowledge of the spectral behavior of

burned vegetation are applied to the resulting Z-score time series. Candidate change observations are those for MODIS band 5 where $|Z| \geq Z_{\text{thresh}}$ and where Z is negative, indicating a drop in post-fire band 5 reflectance. Only candidates where band 5 minus band 7 decreases after burning are considered to be burned. This is based on observations that burning causes a reduction in band 5 reflectance but less change in band 7, whereas other non-fire changes, such as flooding, have similar effects in both bands (Roy et al., 2002b). A temporal constraint is used to differentiate between temporary changes considered as noise and fire-affected areas, which have persistently lower post-fire band 5 reflectance.

5. Global algorithm: statistical thesholding

In the global algorithm, we use a more robust Z-score definition that incorporates a fixed estimate of the noise in the new observation:

$$Z_\lambda = \frac{\rho_{\text{new}}(\lambda, \Omega, \Omega') - \rho(\lambda, \Omega, \Omega')}{\varepsilon} \quad (2)$$

$$\varepsilon = \sqrt{\sigma_\lambda^2 + e^2 \frac{1}{w}}$$

where σ_λ is a fixed pre-assigned estimate of the noise in $\rho_{\text{new}}(\lambda, \Omega, \Omega')$ that is assumed to be independent of the error in the predicted reflectance $\rho(\lambda, \Omega, \Omega')$ that is estimated as before as $e^2(1/w)$. We use conservative estimates of σ_λ defined by validation of MODIS land surface reflectance data sensed under low aerosol conditions (Vermote et al., 2002; Vermote, personal communication). The estimates are summarized in Table 1 for the seven MODIS land surface reflective bands. The incorporation of σ_λ reduces the incidence of overestimated Z-score values that occur for (1) when the angular sampling of the observations used in the BRDF inversion are similar to that of the new observation (i.e., when the weight of determination is high and $1/w$ low). Incorporation of σ_λ also desensitizes the Z-score to large e values that occur when observations used in the BRDF inversion are contaminated by shadows or by residual cloud (when e is a poor estimate of noise in the data). We note that although large e may result in a reduced Z-score, this is not guaranteed as $\rho(\lambda, \Omega, \Omega')$ will also be unreliable. For this reason, to ensure that grossly unreliable BRDF inversion results are not used, inversions with e greater than $5\sigma_\lambda$ are discarded.

6. Global algorithm: multiple wavelengths

In the global algorithm, MODIS bands that are sensitive and insensitive to biomass burning are used to detect changes due to fire and to differentiate them from other types of change, respectively. The near-infrared and longer wavelength 500 m land reflectance bands (Table 1) are used because they are generally insensitive to smoke aerosols emitted from vegetation fires (Kaufman & Remer, 1994; Miura et al., 1998). An analysis of the ability of the MODIS land surface reflectance bands to discriminate between recently burned and unburned vegetation is first described followed by discussion of similar spectral changes that are not caused by burning. This is followed by discussion of how multiple MODIS bands are used in the global algorithm.

6.1. Burned–unburned MODIS band separability analysis

The burned–unburned band separability approach described by Roy et al. (2002b) is applied to a month of MODIS data in each study region. In this approach the MODIS 500 m land surface reflectance bands are examined at locations where 1 km MODIS active fires were detected. Only locations where at least three non-cloudy, good quality, low or average aerosol surface reflectance observations (MODIS land surface reflectance user guide, WWW1) sensed in the n days occurring before the active fire detection and in the n days occurring after the fire detection are considered. The values observed in the n days occurring before and after the active fire detection are considered as unburned and burned respectively and their separability is computed. The Bhattacharyya distance separability measure is used as it is bounded, between values of 0 (no separability) and 2 (high separability), and is monotonically related to classification accuracy when probability distribution class models (e.g., maximum likelihood) are used (Fukunaga, 1990). In this study, n is not greater than 10 days to reduce the impact of any charcoal and ash dissipation or phenological vegetation changes. Observations sensed with a view zenith greater than 45° are not used, as the surface area sensed by the MODIS instantaneous field-of-view increases rapidly above this zenith angle (Wolfe et al., 1998) and greater directionality of surface reflectance at high zenith angles may confuse the separability analysis. We note that using a smaller view zenith angle threshold generally increases the burned–unburned separability but at a cost of reducing the number of available observations and so forcing us to set n to a larger number of days, particularly in cloudy regions.

6.1.1. Australia burned–unburned MODIS band separability results

Fig. 5 shows mean ± 1 standard deviation summary statistics of the unburned (top, open circles) and burned (top, filled circles) reflectance values and the corresponding Bhattacharyya distances (bottom) computed from more than 11,000 MODIS 500 m pixels across the Australian study region. MODIS reflectance data acquired 6 days

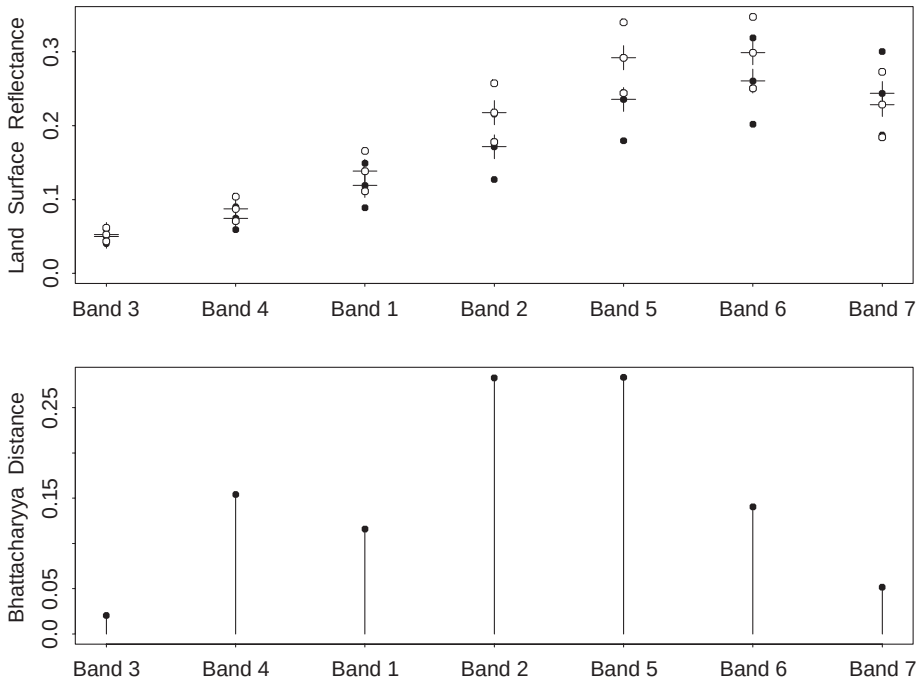

Fig. 5. Australia study region burned–unburned MODIS band separability results. Top: unburned (open circles) and burned (filled circles) land surface reflectance summary statistics for the seven MODIS reflective bands. Mean reflectance (circle superimposed on cross) and mean ± one standard deviation reflectance (circles without crosses) values are shown. Bottom: burned–unburned separability of the reflectance data for the seven MODIS land surface reflectance bands. Data computed from a month of 2002 burned and unburned values at 11,119 500 m pixel locations across the study region. MODIS bands shown in order of increasing wavelength (Table 1).

before and 6 days after active fire detections are considered. Burning reduces the mean land surface reflectance in all MODIS land reflectance bands, except band 7, although changes for bands 3, 4, 1, and 7 are small. The band 6 unburned and burned reflectance data are widely distributed which reduces the band 6 separability, despite the relatively larger drop in reflectance compared to bands 4 and 1, which have comparable separability values. MODIS bands 2 and 5 have the highest separabilities (Bhattacharyya distance ~0.29) and the band 7 separability is low.

6.1.2. South America burned–unburned MODIS band separability results

Fig. 6 shows the south American results computed from 725 MODIS 500 m pixels. Persistent cloud reduced the number of available pixels so that MODIS reflectance data acquired up to 10 days before and 10 days after the fire detections are considered. Fig. 6 illustrates that burning reduces the mean land surface reflectance for bands 2 and 5, slightly reduces band 6 reflectance and increases the reflectance for the other bands. Unlike the other study regions, the band 6 separability is small (less than the band 7 separability). The physical reason for this is unknown, although we note that the highest band separabilities, found for bands 2 and 5, are themselves small (Bhattacharyya distance ~0.12). These low separabilities suggest that mapping fire-affected areas with MODIS 500 m reflectance data may be less successful here than in the other study regions. This is discussed further in the Results section of this paper (Section 10).

6.1.3. Russian Federation burned–unburned MODIS band separability results

Fig. 7 shows results computed from 235 MODIS 500 m pixels distributed across the Russian Federation study region. MODIS reflectance data acquired 8 days before and 8 days after active fire detections are considered. The results illustrated in Fig. 7 are similar to those for Australia, with low band 7 separability and the highest separabilities provided by MODIS band 5 (Bhattacharyya distance ~0.5) and then bands 2 and 6. The separabilities and the reflectance drop due to burning for bands 2, 5, and 6 are considerably higher than for the other study regions. This is not unexpected as boreal forest fires burn high fuel loads to generally leave persistent and spectrally distinct fire-affected areas.

6.1.4. Southern Africa burned–unburned MODIS band separability results

Southern Africa band separability results are described in Roy et al. (2002b) from the analysis of MODIS land surface reflectance data acquired 4 days before and after active fires detected at approximately 15,000 pixels across the region. For all bands burning reduced the mean land surface reflectance, although for bands 1, 3, 4, and 7, the difference between the mean unburned and burned reflectance values was small compared to the standard deviations of these data. MODIS band 5 provided the highest burned–unburned

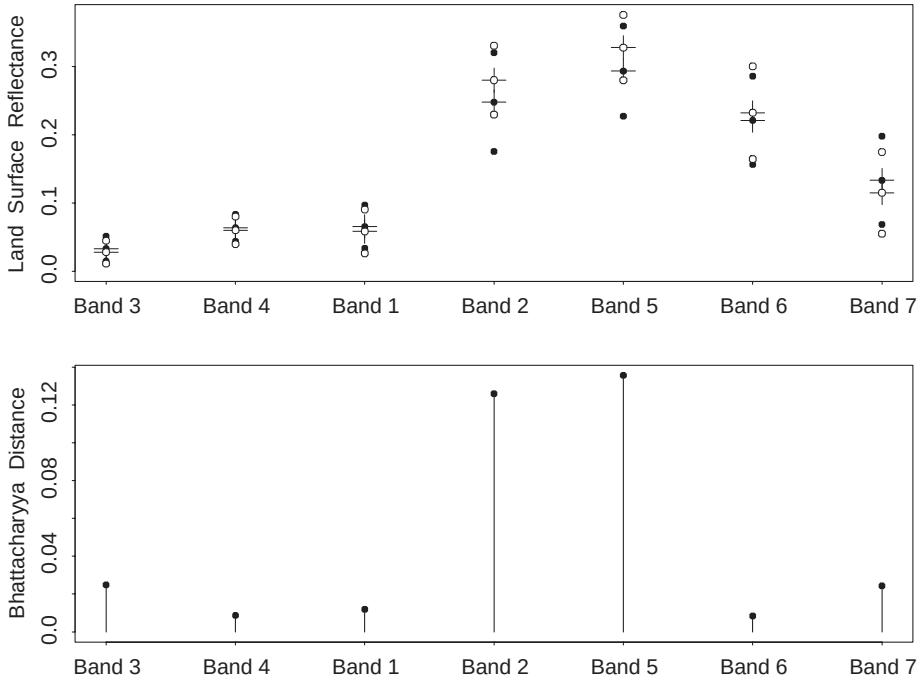

Fig. 6. South America study region burned–unburned MODIS band separability results. Top: unburned (open circles) and burned (filled circles) land surface reflectance summary statistics for the seven MODIS reflective bands. Mean reflectance (circle superimposed on cross) and mean ± one standard deviation reflectance (circles without crosses) values are shown. Bottom: burned–unburned separability of the reflectance data for the seven MODIS land surface reflectance bands. Data computed from a month of 2002 burned and unburned values at 725 500 m pixel locations across the study region.

discrimination (Bhattacharyya distance ~0.35) followed by band 2 and band 6. MODIS band 7 provided little burned–unburned discrimination. Similar observations have been made by less extensive studies undertaken in southern Africa (Sa et al., 2003), Brazil, and North America (Li et al., 2004).

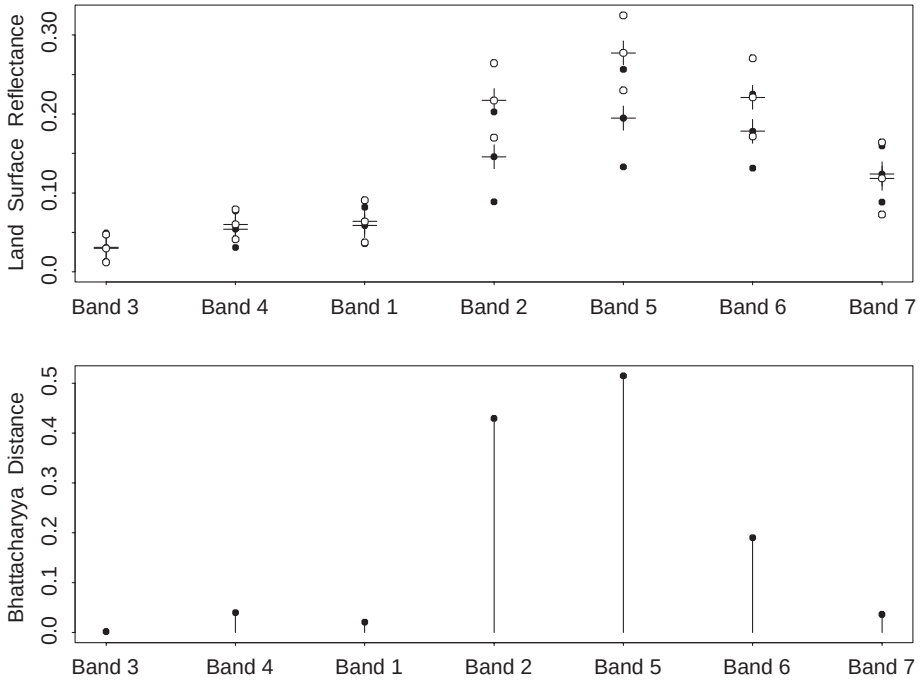

Fig. 7. Russian Federation study region burned–unburned MODIS band separability results. Top: unburned (open circles) and burned (filled circles) land surface reflectance summary statistics for the seven MODIS reflective bands. Mean reflectance (circle superimposed on cross) and mean ± one standard deviation reflectance (circles without crosses) values are shown. Bottom: burned–unburned separability of the reflectance data for the seven MODIS land surface reflectance bands. Data computed from a month of 2002 burned and unburned values at 235 500 m pixel locations across the study region.

6.2. Confusing spectral changes not associated with biomass burning

Some surface changes not associated with biomass burning may exhibit similar spectral changes as those caused by fire. Depending on the algorithm and wavelengths used this may cause false detections (i.e., fire-affected area commission errors). Potentially confusing spectral changes may be inferred from examination of Fig. 8. This figure shows the mean reflectance of 25 cloud-free, near-nadir 500 m MODIS pixels located in the four study regions for a number of different surface types. The data are illustrated in order of increasing wavelength to illustrate the reflectance spectra of snow (light blue), evergreen tropical forest (magenta), bright and dark soil (black solid and dashed lines respectively), water (blue), and herbaceous plants sensed on different dates at the same locations in Australia (green lines) and similarly for grass in Zambia (orange lines).

Most researchers note that burning decreases infrared reflectance shortly after burning (Pereira et al., 1997), which is apparent in our MODIS results illustrated for the different study areas (Figs. 5–7) and for southern Africa (Roy et al., 2002b). Examination of Fig. 8 indicates that decreases in near-infrared and short wave infrared reflectance (MODIS bands 2 and 5) similar to those caused by burning may also occur with snow melt, vegetation removal exposing less reflective soil (e.g., due to harvesting or pests), flooding, and vegetation senescence. The Australian herbaceous plant spectra (green) show a typical reduction in the near-infrared (bands 2 and 5) and increase in red (band 1) reflectance as the vegetation senesces from lush green vegetation to dried material with 100% cover (personal communication, Grant Allan, The Bushfire Council, Alice Springs, Australia). The Zambian grass spectra (orange) show an opposite change and are included to illustrate the complexity of potential sources of spectral confusion. In the Zambia case, senescence from green, waterlogged grass (dashed orange) to dry grass on an exposed bright soil background (solid orange) (personal communication, Joeseph Kanyanga, Zambian Meterological Department, Lusaka, Zambia) increases the near-infrared and the other MODIS band reflectance. The Zambian example illustrates that increasing plant water content (e.g., due to leaf flushing caused by a sudden rainfall event) may reduce MODIS bands 5, 6, and 7 reflectance but have less impact on band 2 reflectance (Fensholt & Sandholt, 2003; Zarco-Tejada et al., 2003). Shadows, cast by clouds and surface relief, are not illustrated in Fig. 8, but generally reduce reflectance in all reflective bands (Holben & Justice, 1981) and so exhibit similar spectral changes as those caused by fire (Roy et al., 2002b).

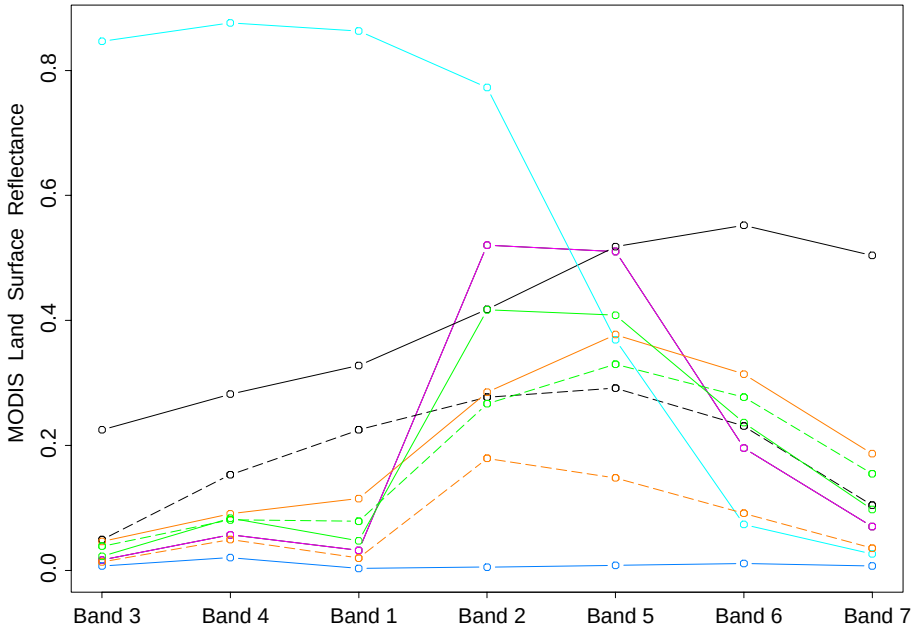

Fig. 8. Illustrative MODIS reflectance band spectra. Light blue: snow (Siberia, April 21st, 2002), magenta: evergreen tropical forest (Mato Grosso, Brazil, August 28th, 2002), black solid line: bright soil (Kalahari sand, northern Namibia, July 8th, 2002), black dashed line: dark soil (Simpson Desert, Australia, September 19th, 2002), green solid line: 100% cover herbaceous plants NDVI=0.8 on dark soil (March 10th, 2002), green dashed line: 100% cover herbaceous plants NDVI=0.5 (April 20th, 2002) (both green lines illustrate the same location, Barkly Tablelands, Northern Territory, Australia), orange solid line: dry senescent grass on bright Kalahari sand NDVI=0.4 (July 28th, 2002), orange dashed line: green grass on waterlogged Kalahari sand NDVI=0.8 (April 7th, 2002) (both orange lines at the same location, Zambezi floodplain, Zambia), blue=water (Lake Argyle, western Australia, September 27th, 2002). MODIS bands shown in order of increasing wavelength (Table 1). Each point shows the mean surface reflectance of 25 cloud-free, near-nadir (view zenith<15°) 500 m MODIS pixels extracted from single date MODIS data sets over homogeneous surfaces.

6.3. Algorithm multi-band implementation

The results illustrated in Figs. 5–7 confirm more globally the southern Africa findings of Roy et al. (2002b) that of the seven MODIS land surface reflectance bands, MODIS bands 5 and 2 provide the highest burned–unburned discrimination and MODIS band 7 provides little discrimination. They confirm that bands 5, 2, and 6 reflectance decrease immediately, and for many days, after burning, and that band 7 reflectance changes relatively less. This spectral knowledge and knowledge of spectrally similar changes that are not associated with burning are incorporated into the global algorithm.

In the global algorithm, drops in both MODIS bands 2 and 5 surface reflectance are used, via (2), to detect candidate changes associated with burning. Tests for these two bands are combined using logical operators:

$$(Z_{\text{band 2}} < -Z_{\text{thresh}} \text{ or } Z_{\text{band 5}} < -Z_{\text{thresh}}) \quad (3)$$

where Z_{band} is the Z-score defined (2) and Z_{thresh} is a fixed wavelength independent threshold. Application of (3) with increasing Z_{thresh} decreases the number of detected burn candidates. The addition of band 2 reduces algorithm sensitivity to unmodeled noise and provides a way to accommodate a bad MODIS Terra band 5 detector that removes a 500 m band 5 scan line every 10 km. If band 5 data are not available due to a bad detector, then (3) is implemented with respect to band 2 only. The Z_{thresh} threshold is the only spectral threshold used in the global algorithm. A number of spectral constraints are also applied to remove changes due to unmodeled noise and non-fire related changes. These are described below.

The original algorithm labeled change candidates as burned if band 5 minus band 7 decreased after burning. This was implemented by comparing nadir bi-directional modeled reflectances computed for these bands before and after the change. In the global algorithm, this constraint is implemented as (4) to remove the need to compute post-change nadir bi-directional modeled reflectance, which may not be possible if there are insufficient observations to invert the BRDF model. In the global algorithm, we also add the constraint that the difference between band 2 and band 7 must decrease:

$$\rho(\lambda_{\text{band 5}}, \Omega, \Omega') - \rho(\lambda_{\text{band 7}}, \Omega, \Omega') > \rho_{\text{new}}(\lambda_{\text{band 5}}, \Omega, \Omega') - \rho_{\text{new}}(\lambda_{\text{band 7}}, \Omega, \Omega') \quad (4)$$

and

$$\rho(\lambda_{\text{band 2}}, \Omega, \Omega') - \rho(\lambda_{\text{band 7}}, \Omega, \Omega') > \rho_{\text{new}}(\lambda_{\text{band 2}}, \Omega, \Omega') - \rho_{\text{new}}(\lambda_{\text{band 7}}, \Omega, \Omega')$$

where $\rho_{\text{new}}(\lambda, \Omega, \Omega')$ is the new reflectance observation that passed (3) and $\rho(\lambda, \Omega, \Omega')$ is the model predicted reflectance computed by inversion of the BRDF model against $m \geq 7$ previous reflectance observations. Addition of band 2 reduces sensitivity to unmodeled noise. Addition of band 2 also helps to remove changes associated with increasing plant water content which is negatively related to bands 5 and 7 reflectance but not band 2 reflectance (Fensholt & Sandholt, 2003; Zarco-Tejada et al., 2003).

A new constraint is used to remove remaining non-fire related changes that pass (3) and (4). Candidate burned pixels are constrained to be only those where:

$$\frac{\overline{\rho_{\text{prev}}}(\lambda_{\text{band 6}}, \Omega, \Omega') - \overline{\rho_{\text{prev}}}(\lambda_{\text{band 7}}, \Omega, \Omega')}{\overline{\rho_{\text{prev}}}(\lambda_{\text{band 6}}, \Omega, \Omega') + \overline{\rho_{\text{prev}}}(\lambda_{\text{band 7}}, \Omega, \Omega')} > \frac{\rho_{\text{new}}(\lambda_{\text{band 6}}, \Omega, \Omega') - \rho_{\text{new}}(\lambda_{\text{band 7}}, \Omega, \Omega')}{\rho_{\text{new}}(\lambda_{\text{band 6}}, \Omega, \Omega') + \rho_{\text{new}}(\lambda_{\text{band 7}}, \Omega, \Omega')} \quad (5)$$

where ρ_{new} is the new reflectance observation that passed (3) and (4), and $\overline{\rho_{\text{prev}}}$ is the median of the three preceding reflectance observations in the time series. The median of the three preceding reflectance observations, rather than the preceding reflectance observation, is used in order to reduce sensitivity to noise occurring in any single preceding observation. A ratio spectral index (5) is used rather than a constraint of the form (4) because shadows, solar illumination, and topographic induced variations that cause proportionally similar reflectance reductions in the different MODIS bands will pass (4), whereas their impact is largely reduced by using a ratio spectral index (Holben & Justice, 1981). Constraint (5) also removes many of the spectrally confusing non-fire related changes illustrated in Fig. 8. This is because MODIS band 6 typically increases when snow melts (Fig. 8, light blue line), vegetation senescences (Fig. 8, green and orange lines), and when certain types of vegetation are removed to reveal more reflective underlying soil (Fig. 8 purple line). In addition, this constraint takes advantage of the generally lower MODIS band 7 reflectance of most surfaces compared to band 6 (Figs. 5–8), whereas black ash has higher band 7 reflectance than band 6 (Pereira, 2003; Roy & Landmann, in press). The spectral index is computed from the observed rather than BRDF model predicted reflectances, even though directional effects remain. This is because post-fire reductions in band 6 reflectance can be small and, in some cases, smaller than the root mean squared of the residuals of the band 6 BRDF inversion. This sensitivity is most problematic when attempting to detect small reflectance changes. For example, occurring when only a fraction of the MODIS observation burned and/or when the fire had low combustion completeness (Roy & Landmann, in press).

Flood events are mostly not falsely detected as fire-affected areas because of the large drop that occurs in band 7 and their consequent removal by constraint (4). False detections along land–water interfaces do occasionally occur due to drops in the reflectance time series caused by misregistration and view zenith variations (Roy, 2000). We attempt to reduce these by applying a conservative water test to remove pixels with MODIS band 7 reflectance less

than 0.04 AND NDVI less than 0.1. The NDVI test is used because dense green vegetation may have low band 7 reflectance (e.g., Fig. 8).

Finally, we note that (3)–(5) may fail to detect burns where more reflective underlying surfaces (in bands 2, 5, and 6) are exposed by the action of fire. For example, when the fire occurs on highly reflective soil, snow, or understory, and ash/charcoal dissipation by the elements is rapid. Similarly, this may occur when the fires are sufficiently hot to produce highly reflective white ash (Roy & Landmann, in press; Stronach & McNaughton, 1989). At the time of writing, we have insufficient field data to study these potential sources of omission error.

7. Global algorithm: temporal application

In the original algorithm description, it was noted that reliability problems may occur when there are underlying non-fire related changes and/or gaps in the reflectance time series that reduce the ability to capture burning events (Roy et al., 2002b). These issues are generally problematic for the detection of changes associated with land-cover conversion or modification processes (Coppin et al., 2004). To reduce the impact of these issues, five algorithm modifications have been implemented in the global algorithm. They capitalize on the spectral persistence of fire-affected areas and are described below.

7.1. Adaptive window duration

Gaps in the reflectance time series, for example due to cloud cover or bad quality input data, reduce the temporal frequency of Z-score calculations as they reduce the number of windows with sufficient observations for BRDF inversion. For example, Jin et al. (2003) considered the impact of missing MODIS Terra time series data on BRDF inversion and found that globally only 50% of MODIS land pixels were observed 7 or more times under cloud-free conditions over a 16-day period in September 2001.

To reduce the impact of gaps, the duration of the BRDF inversion window is now allowed to increase in an adaptive manner, from a minimum of $n=16$ days up to a maximum of $(n+n_{\text{extra}})$ days, until there are at least 7 observations. When there are fewer than 7 observations, no inversion is performed. In this way, by using an adaptive window duration, more BRDF inversions may be performed in the presence of missing data, providing more opportunities for detecting burning events.

To investigate the global impact of different window durations on obtaining sufficient observations for BRDF inversion, we performed the following statistical analysis. In this analysis, it is assumed that the probability of cloud occurrence is constant within each (1200 km × 1200 km) MODIS tile and that there is no temporal correlation of occurrence probability. If day i has a known probability of being cloudy $P_{\text{cloud}}(i)$ (the proportion of clouds on day i within a given tile), then the probability of a particular combination of k different non-cloudy days being selected from n days is defined from the product of n probabilities as:

$$P_{\text{C}}(j) = \prod_{i \in A} (1 - P_{\text{cloud}}(i)) \prod_{i \in B} P_{\text{cloud}}(i) \quad (6)$$

where A is the set of k non-cloudy days and B is the set of $n-k$ cloudy days (with $A \not\subset B$). The probability of there being k different non-cloudy days selected from n days is:

$$P_k^n = \sum_{j=1}^{{}^nC_k} P_{\text{C}}(j) \quad (7)$$

where ${}^nC_k$ is the total number of combinations ($\frac{n!}{(n-k)!k!}$) that k different days can be selected from n days. The probability of there being 7 or more non-cloudy observations selected from n days is then $\sum_{k=7}^{n} P_k^n$.

We applied this approach with $P_{\text{cloud}}(i)$ derived from metadata values stored in the daily Terra MODIS land products (Roy et al., 2002a) that define the fraction of land pixels in each tile flagged as “cloudy” or “uncertain clear” by the MODIS cloud mask algorithm (Ackerman et al., 1998). We derive, independently for each tile, summary statistics on the probability of obtaining k or more non-cloudy observations from an n-day window moved in daily steps through a year of $P_{\text{cloud}}(i)$ values. As cloud cover has high temporal variability, we also derive the percentage of windows over the year where the probability of obtaining k or more non-cloudy observations is greater than a certain probability.

Fig. 9 shows illustrative tile-level results computed for a 16-day window (left column) and a 32-day window (right column) moved in daily steps through the 366 days of 2004. The figure illustrates for each tile the mean annual probability of obtaining 7 or more non-cloudy observations (top row) and the percentage of windows over the year where the probability of obtaining 7 or more non-cloudy observations is greater than 0.9 (bottom row). The results are shown for the 143 MODIS tiles that cover 25% or more land pixels not including Antarctica. Evidently, increasing the window duration increases the probability of there being 7 or more observations. Considering these tiles only, the global mean annual probability of obtaining 7 or more non-cloudy observations increases with window duration from 0.64 ($n=16$ days), 0.83 ($n=24$ days) to 0.91 ($n=32$ days). Similarly, the global mean percentage of windows over the year where the probability of obtaining 7 or more non-cloudy observations is greater than 0.9 increases from 43.2% ($n=16$ days), 68.1% ($n=24$ days) to 82.5% ($n=32$ days). Regional variations are clearly evident, with a reduced number of windows with 7 or more observations in cloudy regions of equatorial West Africa, equatorial South America, Southern and Southeast Asia, and in Boreal regions of Eurasia and Canada.

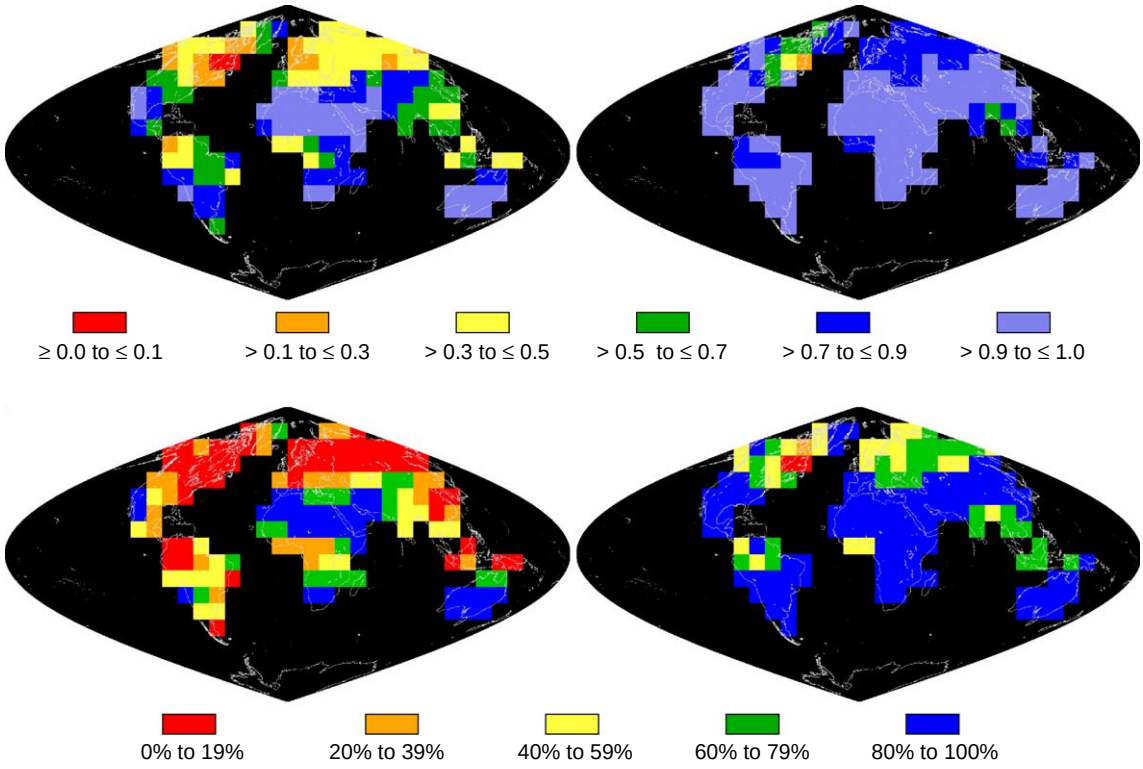

Fig. 9. Global analysis of the impact of increasing temporal window duration on the availability of 7 or more non-cloudy MODIS observations in a 16-day window (left column) and a 32-day window (right column) moved in daily steps through 366 days of 2004. Top row: mean annual probability of obtaining seven or more non-cloudy observations. Bottom row: percentage of windows over the year where the probability of obtaining seven or more non-cloudy observations is greater than 0.9. Results illustrated for 143 MODIS land tiles that cover ≥25% land pixels (not including Antarctica). Each tile has fixed earth locations covering an area of approximately 1200 × 1200 km (10° × 10° at the equator).

7.2. Multi-date prediction

Gaps in the reflectance time series also reduce the number of observations available for prediction. To reduce this impact, the *Z*-score is computed not just for the subsequent day but for several subsequent days. This multi-date prediction and the adaptive window approach are illustrated in Fig. 10. At each window containing 7 or more observations, the BRDF parameters are used to compute *Z*-scores for the non-missing observations sensed on the following S_{search} days. If within the following S_{search} days, a burn candidate is found, i.e., criteria (3)–(5) are met, then the *Z*-scores continue to be computed for S_{test} days after the first burn candidate.

Identification of the approximate date of burning is constrained by the frequency and occurrence of missing observations. To predetermine the precision of this date, each observation in the search duration is considered only if it occurs no more than N_{gap} days after the previous observation. Similarly, the first observation in the search

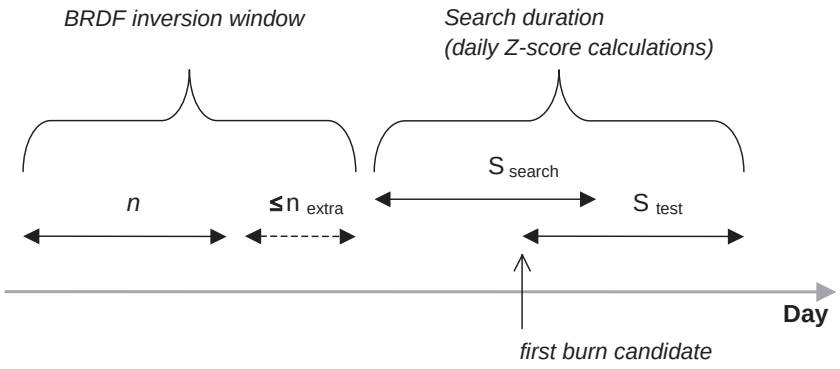

Fig. 10. Adaptive window duration and multi-date prediction illustrated for a hypothetical time series of daily reflectance observations at a single geolocated pixel. The BRDF model is applied to a window containing at least seven observations over a duration of at least n and no more than $n+n_{extra}$ days. The BRDF model parameters are used to compute *Z*-scores for S_{search} subsequent days starting from the first day after the inversion window and, if a burn candidate is found, for the subsequent S_{test} days starting from the first burn candidate.

duration is considered only if it occurs within N_{gap} days of the last observation in the inversion window. In this way, the date of fire occurrence is defined with a precision of N_{gap} days.

The process illustrated in Fig. 10 is repeated moving through the time series in daily steps. *Z*-scores may be computed for an observation by up to S_{search} different inversion windows. A data structure is used to store for each non-missing observation its burn candidate status (i.e., if it passed criteria (3)–(5) or not), the maximum of the band 2 and band 5 *Z*-scores (2), and the associated BRDF inversion window.

7.3. Temporal consistency constraint

The algorithm is based on the assumption that the surface state remains static. Non-random underlying changes, for example, due to vegetation senescence, will cause the *m* observations used in the BRDF model inversion to be of a changing surface so that the BRDF prediction is less reliable. This may be partly compensated via (2) because the residuals of the *m* observations are increased, and so the *Z*-score may be decreased, and because inversions with *e* greater than $5\sigma_\lambda$ are discarded as they are assumed to provide grossly unreliable BRDF prediction. Underlying changes may also cause the *Z*-scores of subsequent observations to be correlated with the slope of the underlying change (Fig. 11). These issues may lead to false burn candidate detection, depending on the slope of the underlying change and on the temporal frequency of any gaps that increase the inversion window and search durations (Fig. 10). A temporal consistency constraint is implemented to reduce the occurrence of these false detections.

The temporal consistency constraint takes advantage of the overlapping sets of *Z*-score information calculated by consecutive inversion windows. It is based on the principal that, if a burn candidate is detected on a certain day by a given inversion window, then it should also be detected as a burn candidate by a closer window. This is illustrated in Fig. 11. The constraint is implemented by sorting the different burn candidates and the windows that considered them into chronological order. Windows that occur more than the search duration ($S_{search}+S_{test}$ days) away from the candidate (Fig. 10) and windows where there were insufficient observations for BRDF inversion or with *e* greater than $5\sigma_\lambda$ are not considered. For each burn candidate, the preceding windows are considered in reverse chronological order (i.e., in Fig. 11, window B is considered before window A). If a preceding window failed to detect the burn candidate within its search duration, then the *Z*-score results for that burn candidate associated with that window and all preceding windows are removed from consideration. Thus, for each burn candidate, *Z*-score results are only retained for the windows that consistently detected the candidate as burned up to and including the preceding window. For example, in Fig. 11, when considering burn candidates on day 6 onwards the *Z*-scores for days 4 and 5 are rejected because although they were detected as burn candidates by window A, they were not detected as such by window B. This method is attractive in that it does not use thresholds and it requires no knowledge of the type of underlying reflectance change. This constraint also reduces sensitivity with respect to the results (3)–(5) provided by any single inversion window.

In our prototyping, we have found that strict implementation of the temporal consistency constraint may lead to rejection of fire-related changes. This is because cases occur where observations sensed at the onset of a fire have small reflectance change and so were not labeled as burned but the subsequent observations of that location were labeled as burned (presumably because subsequently the fire burned the vegetation more completely or burned a greater area). In addition, cases occur where the edge of a large fire-affected area, or an area with a short-axis dimension smaller or

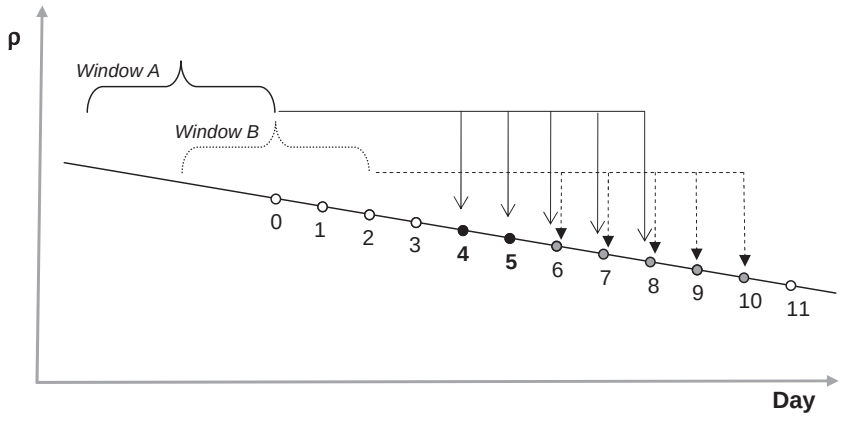

Fig. 11. Illustration of the temporal consistency constraint. A hypothetical non-fire reflectance change with constant slope is shown. Daily reflectance sensed 11 days after inversion window A are shown (circles). Observations with sufficiently large *Z*-scores to be falsely labeled as burn candidates are illustrated (filled circles) for predictions from inversion window A (solid arrows) and from inversion window B (dashed arrows). Window B occurs 2 days after window A. The temporal consistency constraint flags burn candidates on days 4 and 5 as invalid (see text for details). Other windows (not illustrated) similarly flag subsequent burn candidates as invalid.

comparable to the nadir observation dimension, may not be detected at high view zenith angle (Roy, 2000). The temporal consistency constraint is relaxed to accommodate for these cases by allowing for at most one preceding window to fail to detect a candidate as burned.

7.4. Temporal persistency ranking

A temporal persistency constraint was implemented in the original algorithm to differentiate between fire-affected areas and temporary changes, such as shadows, undetected residual clouds, soil moisture changes, and data artifacts, that are considered as noise. Similarly, in the global algorithm, fire-affected pixels are selected from the burn candidates that provide the most persistent evidence of fire occurrence. This is undertaken by considering the Z-scores computed by consecutive inversion windows in a way that accommodates sensitivity to unmodeled noise and sensitivity to gaps in the time series.

For each inversion window (Fig. 10), the day that the first burn candidate was detected ($\text{Day}_{\text{first}}$), the maximum of its bands 2 and 5 Z-scores (Z_{first}), and the total number of observations over the subsequent S_{test} days that were considered ($N_{\text{considered}}$) and detected as burned (N_{pass}), are derived. Different $\text{Day}_{\text{first}}$ candidates may be detected because of sensitivity of the adaptive window duration and multi-date prediction to gaps in the time series. In addition, the same geolocated pixel may burn on separate dates. The results from the different inversion windows are ranked with respect to N_{pass} and then $N_{\text{considered}}$, to provide results in order of the most evidence of persistent burning. If there are results with equal N_{pass} and $N_{\text{considered}}$ values then

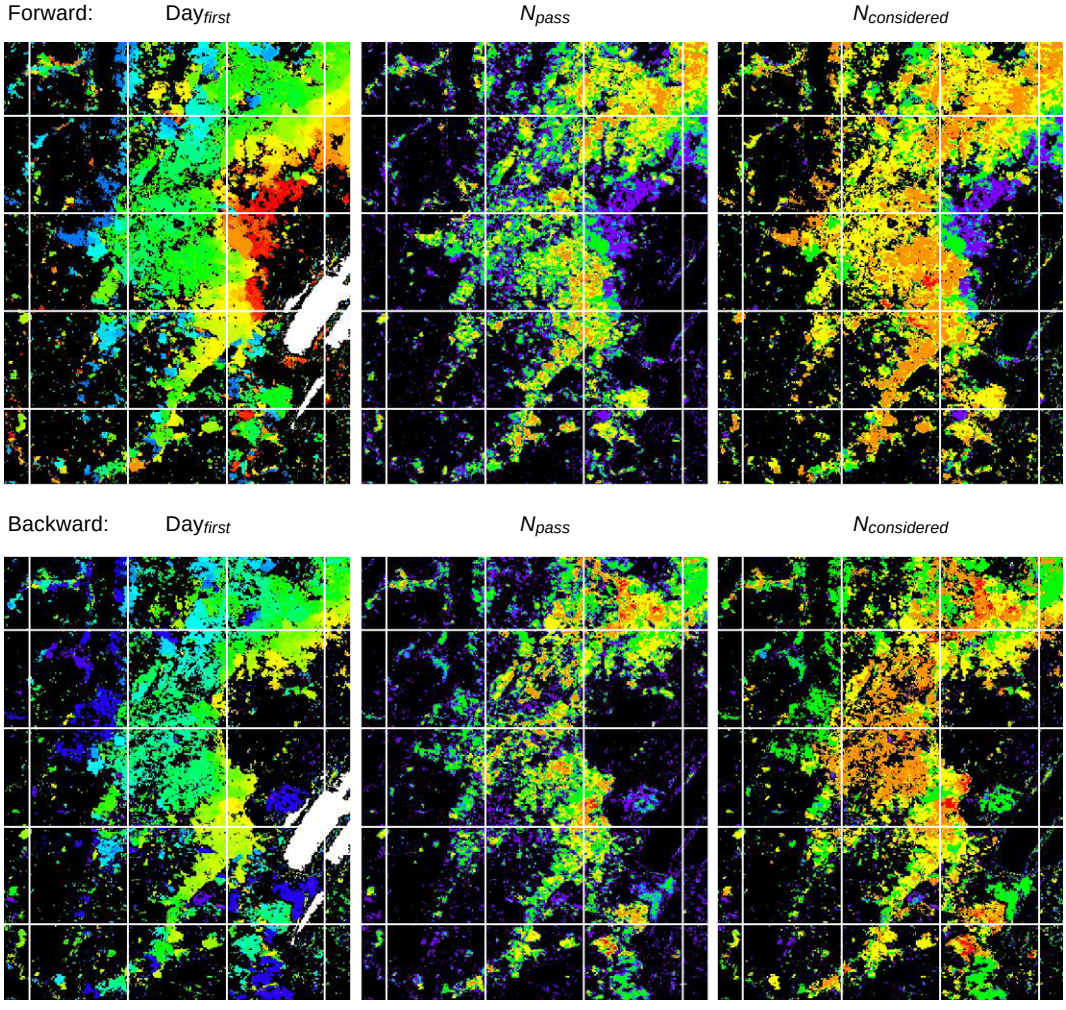

Fig. 12. Example $\text{Day}_{\text{first}}$, N_{pass}, and $N_{\text{considered}}$ results for a 175×225 km area of extensive burning in northern Zambia (gridlines shown every 50 km). These results derived from 75 days of MODIS 500 m land surface reflectance data sensed August 9th to October 23rd, 2002 searching forward in time (top row) and backward in time (bottom row) using the global algorithm and $Z_{\text{thresh}}=3.0$, $S_{\text{search}}=16$ days, $S_{\text{test}}=16$ days, $n=16$ days, and $n_{\text{extra}}=8$ days. The $\text{Day}_{\text{first}}$ values are rainbow color-coded to indicate the day of detected burning (blue = August 9th, red = October 23rd, black no burns detected, white pixels where there were insufficient observations to invert the BRDF model). $\text{Day}_{\text{first}}$ is derived with an 8-day precision ($N_{\text{gap}}=8$ days). The number of observations detected as burned (N_{pass}) and the number of non-missing observations considered ($N_{\text{considered}}$) for $S_{\text{test}}=16$ days after $\text{Day}_{\text{first}}$ are colored as purple: 1–2 days, blue: 3 days, green: 4–6 days, yellow: 7–9 days, orange: 10–12 days, and red: 13–16 days.

the one with the greatest $|Z_{first}|$ is ranked as more persistent. These data are used in a final burn candidate selection procedure described in Section 8.

7.5. Forward and backward change detection

Gaps in the reflectance time series may occur in a non-random manner (for example, due to persistent cloud). Searching both forwards and backwards in time allows burn candidates to be detected in the S_{search} days preceding or following periods of persistently missing data. This also allows burn candidates to be detected in the first and last S_{search} days of the time series. Results for the forward and backward directions are derived independently. When searching backwards in time, an increase in reflectance in the appropriate MODIS bands is searched for rather than a reflectance decrease. The backward direction results are considered less reliable than the forward direction results as the BRDF model inversion may have been applied to changing post-fire reflectance (associated, for example, with ash and charcoal dissipation and/or vegetation regrowth).

Fig. 12 illustrates Day_{first}, N_{pass}, and $N_{considered}$ values derived in the forward and backward directions over a 75-day period for an area of extensive burning in Zambia. The values for the most persistent burn candidates (found by ranking candidates with respect to N_{pass}, $N_{considered}$, and $|Z_{first}|$) are illustrated. The Day_{first} results are colored with a rainbow color scale to indicate the approximate day of burning, with black to indicate no detected burning, and white to show pixels where throughout the time series there were insufficient observations to invert the BRDF model (in this example, due to discarded water observations over Lake Bangweulu). The spatio-temporal progression of burning is clearly evident. The Day_{first} values in the forward and backward directions are spatially and temporally coherent, even though they were derived independently at each pixel. Burns that were detected at the end (red) and at the beginning (blue) of the 75-day period are only evident in the forward and backward directions respectively because they occurred in first and last S_{search} days of the time series. For these burns, the corresponding N_{pass} and $N_{considered}$ values are small because of the smaller number of observations succeeding or preceding the burn in the forward and backwards directions, respectively. The N_{pass} and $N_{considered}$ values also depend on the frequency and occurrence of gaps in the reflectance time series and the occurrence of the burn candidate relative to the non-missing data.

8. Global algorithm: burn candidate selection

The global algorithm attempts to reduce errors of commission by only selecting fire-affected pixels where there are burn candidates that provide persistent evidence of fire occurrence. As the measured persistence varies depending on gaps in the reflectance time series and the timing of the fire relative to non-missing data, an iterative rather than simple thresholding approach is used. Burn candidates found in both the forward and backward directions are considered.

First, fire-affected pixels are selected as occurring on Day_{first} if:

$$N_{pass} \geq 3 \text{ and } \left(N_{pass}/N_{considered}\right) \geq 0.5 \quad (8)$$

In this way, only candidates are selected where at least 3 and 50% of the observations considered over the subsequent S_{test} days are detected as burned. If several burn candidates are found at a given pixel, then they are considered in order of decreasing evidence of persistent burning and the first one that passes (8) is selected. If forward and backward search results have equal persistence, then the forward direction results are given precedence.

Second, rather than discard burn candidates that are likely to be burned but do not pass (8) because of insufficient observations, for example, in Fig. 12 several burned pixels have N_{pass} less than 3 (shown as purple), they are considered using less restrictive criteria than (8) and an iterative search method. This method is based on the principal that there is increasing expectation of a burn occurring in pixels neighboring confidently detected burns (Graetz et al., 2003; Roy et al., 2002b). In this search procedure, the burn candidates selected by (8) are considered seed pixels. Non-seed pixels where burn candidates were detected that did not pass (8) are accepted as burned if they have two or more adjacent seed neighbors and if:

$$/Day_{first} - \overline{Day_{firstseed}}/ < N_{gap} \text{ and } N_{pass} \geq 2 \text{ and } \left(N_{pass}/N_{considered}\right) \geq 0.5 \quad (9)$$

where Day_{first}, N_{pass}, and $N_{considered}$ are the values for the burn candidate that did not pass (8) and $\overline{Day_{firstseed}}$ is the mean Day_{first} value of the two to eight adjacent seed pixels. The N_{gap} constraint ensures that only burn candidates that occur temporally as well as spatially close to the neighboring seed pixels are considered. This procedure is repeated in an exhaustive iterative manner with the pixels that passed (9) being considered as seeds for the next iteration until no more burn candidates that pass (9) can be included. As with (8), if several burn candidates are found at a given pixel, then they are considered in order of decreasing evidence of persistent burning until (9) is met. Again, if forward and backward search results have equal persistence, then the forward direction results are given precedence. Pixels where throughout the time series there were insufficient observations to invert the BRDF model are labeled with a unique code so that they are not subsequently mistaken as being unburned (for example, shown as white in Fig. 1). The temporal thresholds used in (8) and (9) may be varied for regional application, but the ones described here are found to work well for the four study areas using MODIS Terra data.

9. Global algorithm efficiency

The algorithm is computationally expensive compared to conventional approaches. For example, detecting fire-affected areas over a year requires the BRDF inversion and search process (Fig. 10) to be repeated up to $(365-n)$ times for each MODIS land pixel (n is typically 16). Globally, there are approximately 680 million 500 m MODIS land pixels. Computational efficiencies are made by efficient data handling and an efficient BRDF inversion scheme. These are described briefly below.

Data handling efficiencies are made by processing the data on a MODIS tile basis. For each tile, a row of 2400 500 m pixels of the time series input data are read and the algorithm applied for each column within the row using temporal buffers. For each pixel, the window is moved forward through the time series once and the window BRDF parameters are used to search for change in the forward and backward directions rather than moving the window twice through the time series in separate directions. For each window, the tests (3)–(5) are implemented in a sequential manner with no further computation performed if a burn candidate fails a particular test.

Substantive computational savings are found by implementation of an efficient BRDF inversion scheme. The RossThick-LiSparse reciprocal BRDF model describes the bi-directional reflectance as a linear combination of three kernels that are functions of viewing and illumination angles only (Wanner et al., 1997) as:

$$\rho^{\text{obs}} = \sum_{i=1}^{3} (C_i K_i) + \varepsilon \tag{10}$$

where ρ^{obs} is the observed surface spectral directional reflectance, C_i is the weight for each of three kernels K_i (K_1, isotropic kernel; K_2, geometric-optical kernel; K_3, volumetric kernel), and ε is the observation noise. The kernel values K_i are precomputed for the solar and illuminations angles of each observation in the time series and stored in a look up table rather than being recomputed for each inversion window. Eq. (10) is inverted analytically against m reflectance observations using the method of least squares (Whittaker & Robinson, 1960) as:

$$C_{3\times 1} = \left(K^T_{3\times m} K_{m\times 3}\right)^{-1} K^T_{3\times m} \rho^{\text{obs}}_{m\times 1} \tag{11}$$

Since the isotropic kernel $K_1 \equiv 1$, the solution C can be written as an analytical expression of the following eight terms:

$$\sum K_2,\ \sum K_3,\ \sum K_2^2,\ \sum \left(K_3^2\right),\ \sum (K_2 K_3),\ \sum \rho^{\text{obs}},$$
$$\sum \left(\rho^{\text{obs}} K_2\right),\ \sum \left(\rho^{\text{obs}} K_3\right) \tag{12}$$

where $\sum$ represents summation over m observations. Thus, at each step of the moving window algorithm, these terms are re-calculated by the addition of the observation that has just entered the window and the subtraction of the observation no longer in the window. In this more efficient implementation, after the first window has been inverted, subsequent windows may be inverted using elements needed for (11) calculated using $(m-2)/m$ fewer mathematical operations. In practice, due to missing data, more than one observation may be added or subtracting at consecutive window locations reducing this computational saving.

10. Illustrative results

Figs. 1–4 show a month or more of fire-affected areas mapped using the global algorithm. The results exhibit a seasonally expected distribution of burning that is particularly evident in Figs. 1 (southern Africa), 2 (Australia), and 4A (Russian Federation, Arctic Circle). The results were generated with $Z_{\text{thresh}}=3.0$, $S_{\text{search}}=16$ days, $S_{\text{test}}=16$ days, $n=16$ days, $n_{\text{extra}}=8$ days, and $N_{\text{gap}}=8$ days. These parameter values provide reliable fire-affected area results across the four study regions, although improvements can be made locally by reducing the parameter values where missing and/or noisy observations occur infrequently. Setting $Z_{\text{thresh}}=3.0$ detects only those reflectance changes (3) that fall outside of the expected reflectance variation modeled from previous values (the probability that $Z<-3.0$ is ~ 0.0013). Reducing Z_{thresh} below 3.0 decreases omission errors but introduces proportionally greater commission errors across the study regions. The reasons for this are complex and are related to factors including the relative degree of reflectance change post-fire and the spectral persistence of this change, the frequency and occurrence of gaps or noisy observations, the timing of the fire relative to the non-missing data, and the adaptive window duration and multi-date prediction parameters. The parameters S_{search}, S_{test}, and n are set equal to the MODIS 16-day repeat cycle (Wolfe et al., 2002) in an attempt to maximize variation in the MODIS viewing geometry. This is desirable for reliable BRDF model inversion although is not critical for reflectance prediction under similar MODIS sensing and illumination geometries (Roy et al., 2002b). The n_{extra} parameter is set to 8 days to give a BRDF window duration of 16 to 24 days, which provides sufficient observations for BRDF inversion over all but the most persistently cloudy parts of the study regions. The N_{gap} parameter is set arbitrarily to 8 days to accommodate more than a week of persistently missing observations and so that the date of burning is derived with a precision of no worse than 8 days.

Figs. 13–16 illustrate spatial subsets of the study region results shown in Figs. 1–4 at larger scale. Contemporaneous MODIS 1 km day and night active fire detections are illustrated for comparative purposes. These independently derived fire products exhibit a similar, locally coherent, spatio-temporal progression of burning. Generally, a high correspondence is observed between the *locations* and *dates* of the 500 m fire-affected area results and the cumulative 1

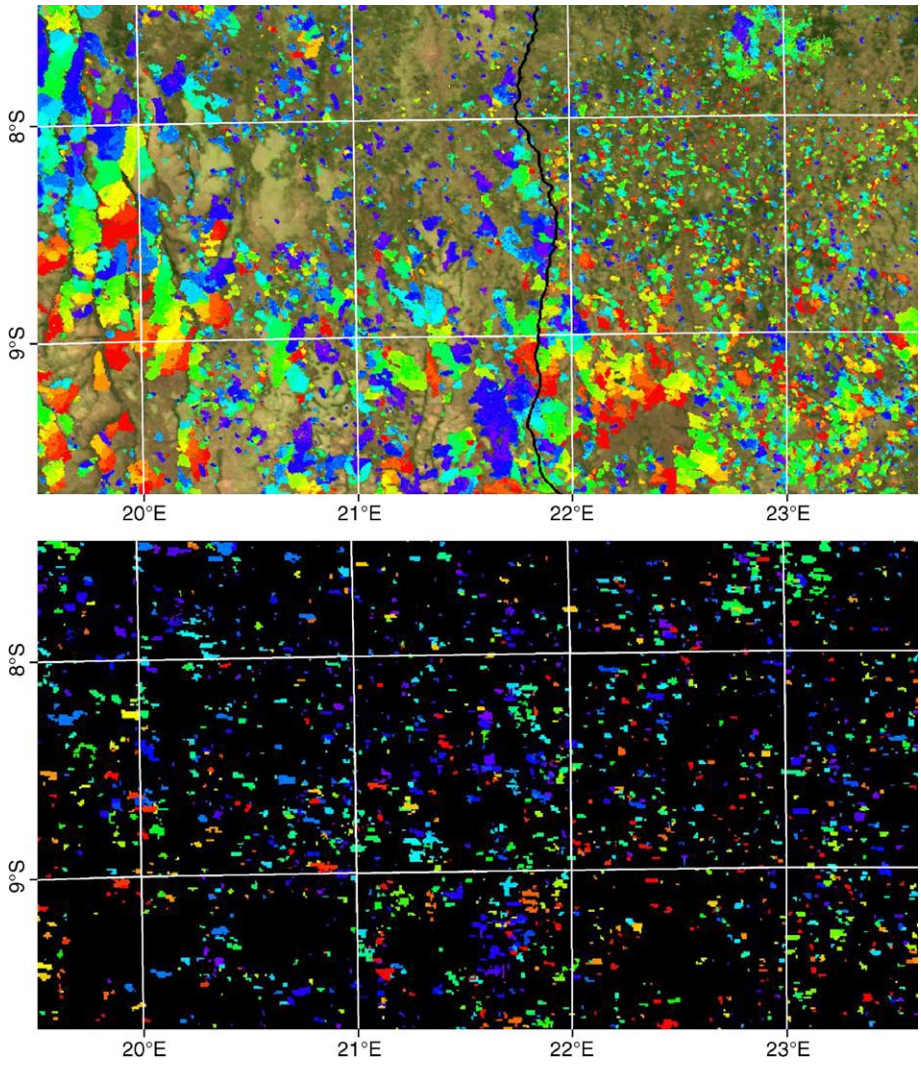

Fig. 13. Example southern Africa results showing a 450 × 250 km region encompassing the border between Angola and the Democratic Republic of Congo. The colors illustrate 1.5 months of extensive burning from June 23rd (violet) to August 8th (red), 2002 detected by the 500 m MODIS fire-affected area product (top) and the 1 km MODIS day and night active fire product (bottom). The MODIS fire-affected areas (top) are shown superimposed on 500 m MODIS nadir bi-directional modeled red (0.645 μm), green (0.555 μm), and blue (0.469 μm) reflectance to provide geographic context (country borders shown black). See Fig. 1 for equivalent continental results. Where the MODIS active fire detections (bottom) are black, no fires were detected (and the percentage of MODIS day and night 1 km observations labelled as cloudy over the mapped period were ≤10%).

km active fire detections. Product differences are evident among the study regions and are described below. The MODIS active fire product has errors of omission of commission that are still being quantified globally (Morisette et al., in press) and so this product intercomparison is not a surrogate for validation.

The results for southern Africa (Fig. 13) and Australia (Fig. 14) are similar in that substantially more fire-affected areas are detected by the global fire-affected area algorithm than by the cumulative day and night 1 km active fire detections. The proportion of the illustrated areas that the global algorithm labeled as burned are 35.7% for southern Africa and 20.5% for Australia, approximately three times greater than the proportion labeled as burned by the cumulative active fire detections (9.1% and 6.6% for southern Africa and Australia, respectively). In both examples, fewer than 10% of the day and night MODIS active fire observations were obscured by cloud. Consequently, active fire under-detection may be attributed to MODIS overpassing at times when the fires were not actively burning and/or to the active fires being insufficiently hot or large for their detection (Justice et al., 2002b; Giglio et al., 2003). The southern Africa results (Fig. 13) include a minority of locations where active fires were detected but no fire-affected areas were mapped. The reasons for this are varied but include the occurrence of small and/or low combustion completeness fires that caused an insufficiently large change in reflectance (Roy & Landmann, in press) for their detection by the fire-affected area algorithm.

The south America results (Fig. 15) illustrate examples of fire activity where there is relatively low and high forest

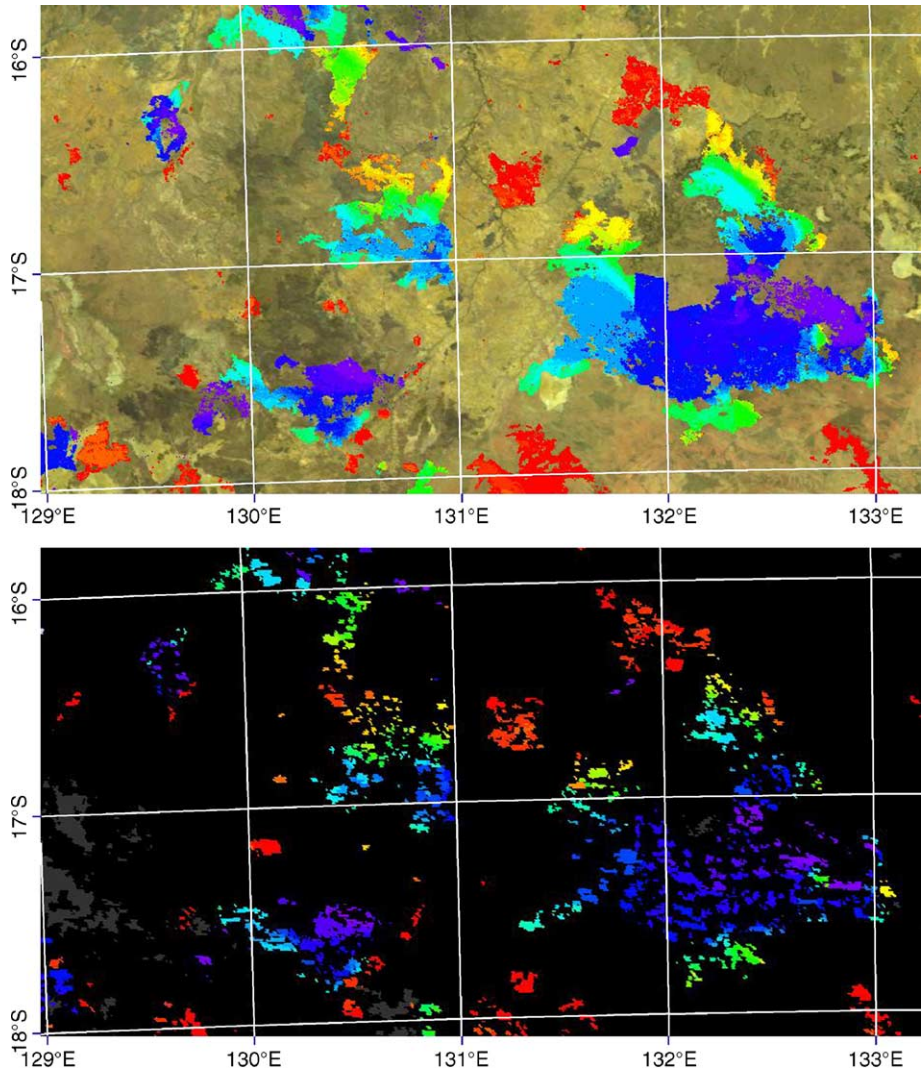

Fig. 14. Example Australian results showing a 450 × 250 km region of the Northern Territory. The colors illustrate 1 month of extensive burning from October 1st (violet) to October 31st (red), 2002 detected by the 500 m MODIS fire-affected area product (top) and the 1 km MODIS day and night active fire product (bottom). The MODIS fire-affected areas (top) are shown superimposed on 500 m MODIS nadir bi-directional modeled red (0.645 μm), green (0.555 μm), and blue (0.469 μm) reflectance to provide geographic context. See Fig. 2 for equivalent larger scale results. The MODIS active fires grey shades (bottom) illustrate locations where no fires were detected and show the percentage of MODIS day and night 1 km observations labelled as cloudy by the MODIS active fire product over the month (black = 0–10%, grey = 11–20%).

cover. The low forest cover results in the Mato Grasso (Fig. 15, top) have similar total area burned differences between the global algorithm and cumulative active fire detections as the southern Africa and Australian results, with a greater area labeled as burned by the global algorithm (5.5%) than by the cumulative active fire detections (2.3%). This contrasts to the high forest cover results in southern Para (Fig. 15, bottom) where a greater area is labeled as burned by the cumulative active fire detections (6.1%) than the global algorithm (4.1%). We believe that the fire-affected area algorithm may be under detecting fires within the forest and along the forest boundaries because reflectance changes are obscured by unburned overstorey vegetation (Alencar et al., 2004). This and the apparently small and spatially fragmented nature of many fire-affected areas (relative to the MODIS 500 m nadir observation dimension) may explain the low south America MODIS burned–unburned separabilities illustrated in Fig. 6. We note that, where fire-affected areas are mapped, their spatial correspondence with the geographic detail evident in the background 500 m land surface reflectance data appears to be higher than that provided by the 1 km active fire product. Certainly, the cumulative active fire detections will overestimate the fire-affected area if the fires are smaller than the MODIS 1 km observation dimension. Without higher spatial resolution remote sensing or ground-based validation data it is difficult to draw any definitive conclusions.

The Boreal forest results (Fig. 16) were derived under more cloudy conditions than the other detailed study region examples; in places up to 30% of the MODIS day and night observations were obscured by cloud. This cloudiness impacts both the active fire and fire-affected area products.

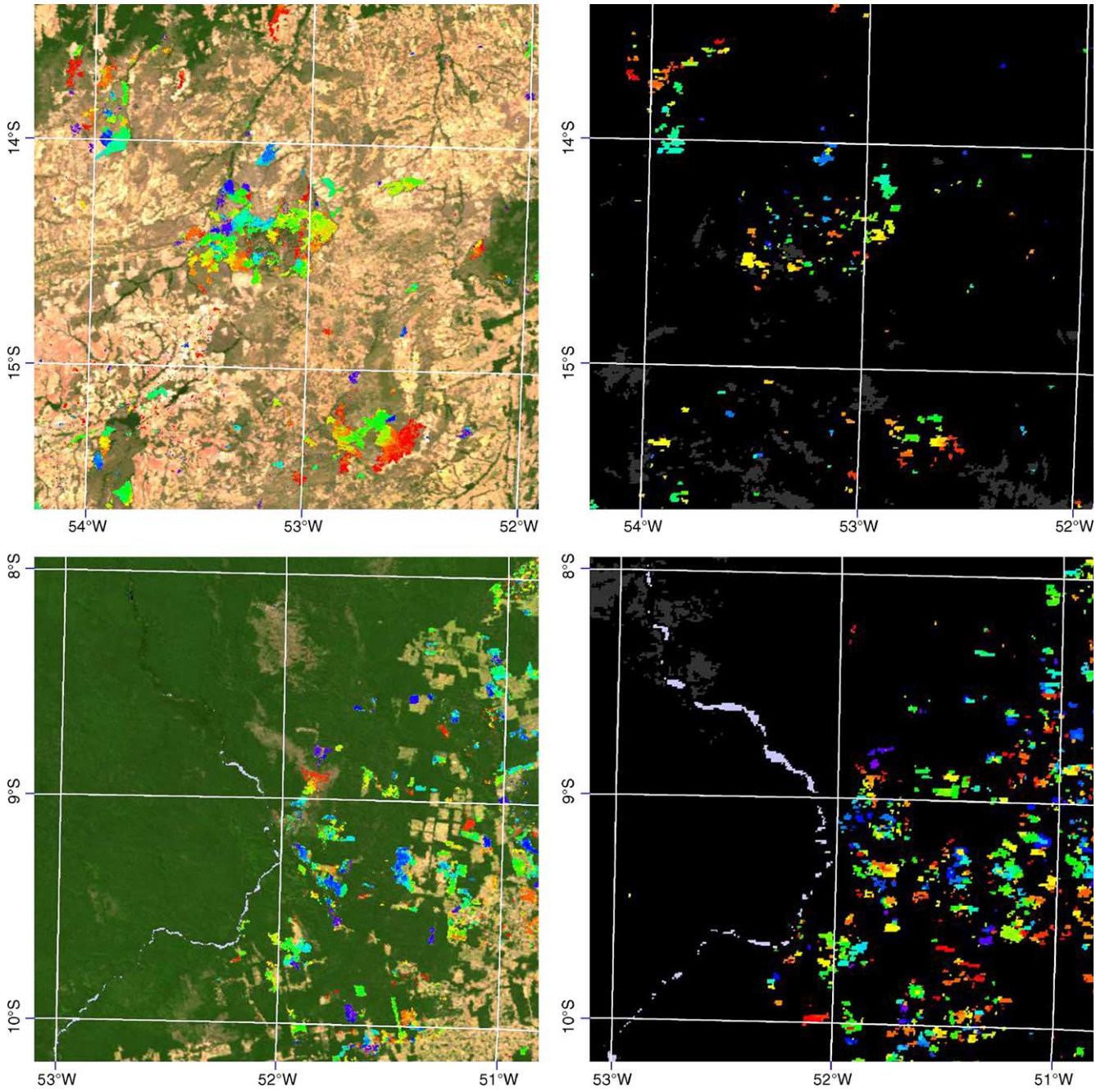

Fig. 15. Example South America results showing two 250 × 250 km regions in Brazil: Mato Grosso (including parts of Serra do Roncador and Planalto do Mato Grosso) (top row) and Southern Para (bottom row). The colors illustrate 1 month of extensive burning from August 1st (violet) to August 31st (red), 2002 detected by the 500 m MODIS fire-affected area product (left column) and the 1 km MODIS day and night active fire product (right column). The MODIS fire-affected areas (left column) are shown superimposed on 500 m MODIS nadir bi-directional modeled red (0.645 μm), green (0.555 μm), and blue (0.469 μm) reflectance to provide geographic context. The Xingu River is colored lilac (bottom row). See Fig. 3 for equivalent larger scale results. The MODIS active fire grey shades (right column) illustrate locations where no fires were detected and show the percentage of day and night 1 km observations labelled as cloudy by the MODIS active fire product over the month (black = 0–10%, grey = 11–20%).

The fire-affected area product generally depicts the large fires in a more spatially cohesive manner than the cumulative active fire detections. Similar total burned areas are mapped by the global algorithm (5.5%) and the cumulative active fire detections (6.1%), but their temporal correspondence is not high. For example, the cluster of fire-affected areas located to the West of longitude 129° E and encompassing latitude 63° N are labeled as occurring at the beginning of July (violet, Fig. 16, top) but were either not detected or were detected approximately a week later by the active fire product (green, Fig. 16, bottom). Locations where no active fires were detected but fire-affected areas were mapped near the beginning or the end of July may be attributed to fire occurrence up to $N_{gap} = 8$ days before or

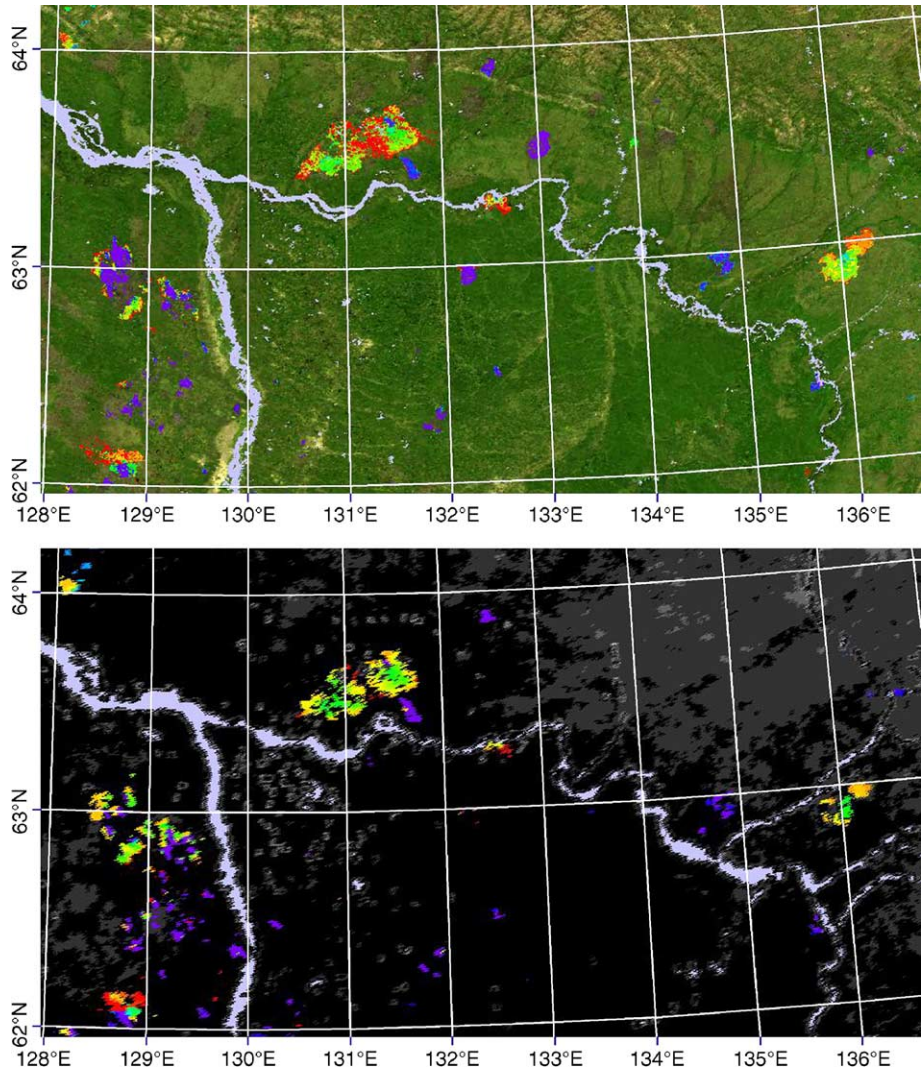

Fig. 16. Example Russian Federation results showing a 450 × 250 km region near the river Lena. The colors illustrate 1 month of extensive burning from July 1st (violet) to July 31st (red), 2002 detected by the 500 m MODIS fire-affected area product (top) and the 1 km MODIS day and night active fire product (bottom). The MODIS fire-affected areas (top) are shown superimposed on 500 m MODIS nadir bi-directional modeled red (0.645 μm), green (0.555 μm), and blue (0.469 μm) reflectance to provide geographic context. See Fig. 4A for equivalent larger scale results. The MODIS active fire grey shades (bottom) illustrate locations where no fires were detected and show the percentage of MODIS day and night 1 km observations labelled as cloudy by the MODIS active fire product over the month (black = 0–10%, dark grey = 11–20%, light grey = 21–30%). Rivers are shown as lilac.

after July. Periods of persistent cloud reduce the ability of the global algorithm to map precisely the date of fire occurrence and clouds preclude active fire detection. Missing active fire detections where fire-affected areas are mapped in the middle of the month, for example, at longitude 134° E and latitude 63.5° N, occur. This example, and others evident in Figs. 13–16, illustrate that algorithms that attempt to "grow" fire-affected areas using morphological operators (Serra, 1986) around the locations of active fire detections may have systematic under-detection issues.

11. Conclusions

We have described in detail an improved algorithm developed for systematic global mapping of fire-affected areas using MODIS 500 m land surface reflectance time series data. It is based on a bi-directional reflectance model-based expectation change detection approach that does not require training data or other sources of information, including human intervention. We have improved on the original algorithm (Roy et al., 2002b) by making the new global algorithm (i) operate on multiple wavebands, (ii) better differentiate between fires and other types of change, (iii) use more robust temporal constraints, (iv) reduce sensitivity to non-random underlying changes and gaps and unmodeled noisy observations, and (v) use spatial contextual information to capture the increased likelihood of fire occurrence near confidently detected fire-affected areas. These improvements serve to derive more robust measures and to better propose the underlying cause of any detected change. The algorithm is potentially applicable to the

mapping of other land-cover conversion or modification processes that are characterized by rapid reflectance change.

We have demonstrated the global algorithm's performance for different fire regimes with results that reveal a coherent spatio-temporal mapping of fire-affected area. The results indicate that the algorithm provides spatial and temporal fire mapping information that complement the information provided by MODIS 1 km active fire detections. The algorithm appears to map the spatial extent of burning more reliably then cumulative MODIS 1 km active fire detections, although in dense topical forest this may not be the case.

The global fire-affected area algorithm detects the approximate date of burning by locating the occurrence of rapid changes in MODIS reflectance time series. Consequently, unlike active fire detection approaches, the global algorithm can map the location and approximate date of burning for fires obscured by cloud or thick smoke, or that were not burning, at the time of satellite overpass. The algorithm cannot map fires however in periods of frequently missing observations—when there were fewer than seven observations occurring over several weeks. Preliminary global cloud analysis indicate that persistent cloud-cover may restrict MODIS fire-affected area mapping in parts of equatorial West Africa, equatorial South America, Southern and Southeast Asia, and Boreal regions in Eurasia and Canada. Active fires may be detected in the few cloud-free observations sensed in frequently cloudy periods. This implies that active fire and fire-affected area products may be used in conjunction to improve fire information depending on cloud conditions.

The global algorithm will be implemented in the MODIS land production system as part of the standard MODIS land product suite (Justice et al., 2002a) to systematically map fire-affected areas globally for the 6+-year MODIS observation record. The resulting 500 m product will map the approximate day of burning and will be made available on a monthly basis. A comprehensive program of validation is under development and international collaborations are being made with regional networks of fire scientists and product users through the GOFC/GOLD program and the CEOS Land Product Validation Working group (Justice et al., 2003; Morisette et al., 2002). A prototype validation protocol has been developed using multi-date Landsat ETM+ data (Roy et al., in press) and validation results for southern Africa and Australia are described in separate papers in preparation. The global algorithm may be enhanced further based on the results of these validation initiatives or if the performance of the MODIS instrument changes. The temporal threshold values used to generate the results presented in this paper may be modified to accommodate regional differences in cloud cover. Additional lines of enquiry are also being investigated, including definition of the algorithm detection limits with respect to factors including the size of the area burned and the completeness of combustion (Roy & Landmann, in press) and the utility of multi-temporal BRDF models that explicitly model surface dynamics (Rebelo et al., 2004).

The bi-directional reflectance model-based expectation change detection algorithm provides a route for the use of multiple data sources and observations of varying degrees of uncertainty within a modeling framework. Early results using both MODIS Aqua and MODIS Terra data demonstrate improvements in fire-affected area mapping realized by incorporating additional angular observations to better constrain the BRDF retrieval and improve cloud-free observation of the surface. The algorithm is applicable to data from other sensors, including future operational sensors such as the National Polar-orbiting Operational Environmental Satellite System (NPOESS) Visible Infrared Imaging Radiometer Suite (VIIRS) which will extend the MODIS data record into the next decade (Townshend & Justice, 2002).

Acknowledgements

This work was funded by the NASA Land Cover and Land Use Change (LCLUC) and Applications Programs (grant NAG511251) and the NASA Earth System Science Program (grant NNG04HZ18C). This work was also conducted in collaboration with the U.K Natural Environment Research Council Centre for Terrestrial Carbon Dynamics. Dr. Sadashiva Devadiga is thanked for coding the intermediate surface reflectance product. Dr. Simon Trigg is thanked for his comments on the revised manuscript. The anonymous reviewers are thanked for their comments.

References

Ackerman, S. A., Strabala, K. I., Menzel, W. P., Frey, R. A., Moeller, C. C., & Gumley, L. E. (1998). Discriminating clear sky from clouds with MODIS. *Journal of Geophysical Research*, *103*, 32141–32157.

Alencar, A. A. C., Solorzano, L. A., & Nepstad, D. C. (2004). Modeling forest understory fires in an Eastern Amazonian Landscape. *Ecological Applications*, *14*(4), 139–149.

Arino, O., & Rosaz, J. (1999). 1997 and 1998 world ATSR fire atlas using ERS-2 ATSR-2 data. *Proceedings of the Joint Fire Science Conference, Boise, Idaho, 15–17 June 1999*, edited by Neuenschwander, L. F., Ryan, K. C., & Golberg, G. E. (Eds), Boise: University of Idaho and the International Association of Wildland Fire, pp. 177–182.

Barbosa, P. M., Grégoire, J. -M., & Pereira, J. M. C. (1999). An algorithm for extracting burned areas from time series of AVHRR GAC data applied at a continental scale. *Remote Sensing of Environment*, *69*, 253–263.

Barnsley, M. J., Allison, D., & Lewis, P. (1997). On the information content of multiple-view-angle (MVA) data sets. *International Journal of Remote Sensing*, *18*, 1937–1960.

Bradstock, R. A., Williams, J. E., & Gill, A. M. (Eds.). (2002). *Flammable Australia: The fire regimes and biodiversity of a continent*. Cambridge, UK: Cambridge University Press.

Bucini, G., & Lambin, E. F. (2002). Fire impacts on vegetation in Central Africa: A remote-sensing-based statistical analysis. *Applied Geography*, *22*, 27–48.

Cahoon, D. R., Stocks, B. J., Levine, J. S., Cofer, W. R., & O'Neill, K. P. (1992). Seasonal distribution of African savanna fires. *Nature*, *359*, 812–815.

Cardoso, M. F., Hurtt, G. C., Moore, B., Nobre, C. A., & Prins, E. (2003). Projecting future fire activity in Amazonia. *Global Change Biology*, *9*, 656–669.

Cihlar, J., Manak, D., & D'Iorio, M. (1994). Evaluation of compositing algorithms for AVHRR data land. *IEEE Transactions on Geoscience and Remote Sensing*, *32*(2), 427–437.

Cochrane, M. A. (2003). Fire science for rainforests. *Nature*, *27*, 913–919.

Cochrane, M. A., Alencar, A., Schulze, M. D, Souza Jr., C. M., Nepstad, D. C., Lefebvre, P., et al. (1999). Positive feedbacks in the fire dynamic of closed canopy tropical forests. *Science*, *284*, 1832–1835.

Committee on Earth Observation Satellites (CEOS). (2000). *The use of earth observing satellites for hazard support: A report of the disaster management support group*. NOAA. 156 pp.

Coppin, P., Jonckheere, I., Nackaerts, K., Muys, B., & Lambin, E. (2004). Digital change detection methods in ecosystem monitoring: A review. *International Journal of Remote Sensing*, *25*, 1565–1596.

Crutzen, P. J., & Andreae, M. O. (1990). Biomass burning in the tropics: Impact on atmospheric chemistry and biogeochemical cycles. *Science*, *250*, 1669–1678.

Crutzen, P. J., & Goldammer, J. (1993). *Fire in the environment; its ecological, climatic and atmospheric chemical importance*. Chichester: John Wiley and Sons.

Csiszar, I., Justice, C. O., Mcguire, A. D., Cochrane, M. A., Roy, D. P., Brown, F., et al. (2004). Land use and fires. In Gutman A., et al., (Eds.), *Land change science: Observing, monitoring, and understanding trajectories of change on the earth's surface*. Kluwer Academic Publishers.

de Miranda, E. E., & John, L. (2000). Monitoring and mapping fires in Brasil current products and information networks. In F. Ahern, J. M. Grégoire, & C. Justice (Eds.), Forest fire monitoring and mapping: A component of global observation of forest cover. *Report of a workshop, November 3–5, 1999* (pp. 159–169). Italy: Joint Research Centre Ispra.

Dozier, J. (1981). A method for satellite identification of surface temperature fields of subpixel resolution. *Remote Sensing of Environment*, *11*, 221–229.

Dyer, R., Jacklyn, P., Patridge, I., Russell-Smith, J., & Williams, R. (Eds.). (2001). *Savanna burning: Understanding and using fire in northern Australia*. Darwin, NT, Australia: Tropical Savannas Cooperative Research Centre.

Elvidge, C. D., Nelson, I., Hobson, V. R., Safran, J., & Baugh, K. E. (2001). Detection of fires at night using DMSP-OLS data. In F. J. Ahern, J. Goldammer, & C. O. Justice (Eds.), *Global and regional wildland fire monitoring from space: Planning a coordinated international effort* (pp. 125–144). The Hague: SPB Academic Publishing.

Eva, H., & Lambin, E. F. (1998a). Burnt area mapping in Central Africa using ATSR data. *International Journal of Remote Sensing*, *19*, 3473–3497.

Eva, H., & Lambin, E. F. (1998b). Remote sensing of biomass burning in tropical regions: Sampling issues and multisensor approach. *Remote Sensing of Environment*, *64*, 292–315.

Fensholt, R., & Sandholt, I. (2003). Derivation of a shortwave infrared water stress index from MODIS near- and short wave infrared data in a semi-arid environment. *Remote Sensing of Environment*, *87*(1), s.111–s.121.

Fraser, R. H., Li, Z., & Cihlar, J. (2000). Hotspot and NDVI differencing synergy (HANDS): A new technique for burned area mapping over boreal forest. *Remote Sensing of Environment*, *74*, 362–376.

Fredericksen, P. S., Langaas, S., & Mbaye, M. (1990). NOAA-AVHRR and GIS-based monitoring of fire activity in Senegal—A provisional methodology and potential applications. In J. G. Goldammer (Ed.), Fire in the tropical biota: Ecosystem processes and global challenges. *Ecological Studies*, *vol. 84* (pp. 400–417). Berlin: Springer-Verlag.

French, N. H., Kasischke, E. S., & Williams, D. G. (2003). Variability in the emission of carbon-based trace gases from wildfire in the Alaskan boreal forest. *Journal of Geophysical Research*, *108*(D1), 8151.

Frost, P. G. H. (1999). Fire in southern African woodlands: Origins, impacts, effects, and control. Proceedings of an FAO Meeting on Public Policies Affecting Forest Fires. *FAO Forestry Paper*, *vol. 138* (pp. 181–205).

Fukunaga, K. (1990). *Introduction to statistical pattern recognition.* Second edition. Netherlands: Academic Press Inc.

Furyaev, V. V. (1996). Pyrological regimes and dynamics of the southern taiga forests in Siberia. In J. G. Goldammer, & V. V. Furyaev (Eds.), *Fire in ecosystems of boreal Eurasia* (pp. 168–185). Netherlands: Kluwer Academic Publishers.

Gao, F., Jin, Y., Xiaowen, L., Schaaf, C. B., & Strahler, A. H. (2002). Bidirectional NDVI and atmospherically resistant BRDF inversion for vegetation canopy. *IEEE Transactions on Geoscience and Remote Sensing*, *40*, 1269–1278.

Gao, F., Schaaf, C., Strahler, A. H., & Lucht, W. (2001). Using a multi-kernel least variance approach to retrieve and evaluate albedo from limited BRDF observations. *Remote Sensing of Environment*, *76*, 57–66.

Giglio, L., Descloitres, J., Justice, C. O., & Kaufman, Y. J. (2003). An enhanced contextual fire detection algorithm for MODIS. *Remote Sensing of Environment*, *87*, 273–382.

Global Climate Observing System (GCOS). (1997). GCOS/GTOS plan for terrestrial climate-related observations. WMO TD 796, GCOS-32, Geneva. 132 pp.

Goldammer, J. G., & Furyaev, V. V. (Eds.). (1996). *Fire in ecosystems of boreal Eurasia*. Dordrecht: Kluwer Academic Pub.

Govaerts, Y., Pereira, J. -M., Pinty, B., & Mota, B. (2002). Impact of fires on surface albedo dynamics over the African Continent. *Journal of Geophysical Research*, *107*, 4629–4633.

Graetz, R. D., Grégoire, J. M., Lovell, J. L., King, E. A., Campbell, S. K., & Tournier, A. (2003). A contextual approach to the mapping of burned areas in tropical Australian savannas using medium-resolution satellite data. *Canadian Journal of Remote Sensing*, *29*(4), 499–509.

Grégoire, J. -M., Tansey, K., & Silva, J. M. N. (2003). The GBA2000 initiative: Developing a global burnt area database from SPOT-VEGETATION imagery. *International Journal of Remote Sensing*, *24*, 1369–1376.

Holben, B. (1986). Characteristics of maximum-value composite images from temporal AVHRR data. *International Journal of Remote Sensing*, *7*, 1417–1434.

Holben, B., & Justice, C. (1981). An examination of spectral band ratioing to reduce the topographic effect in remotely sensed data. *International Journal of Remote Sensing*, *2*, 115–133.

Janetos, A. C., & Justice, C. O. (2000). Land cover and global productivity: A measurement strategy for the NASA program. *International Journal of Remote Sensing*, *21*, 1491–1512.

Jin, Y., Schaaf, C. B., Gao, F., Li, X., Strahler, A. H., Lucht, W., & Liang, S. (2003). Consistency of MODIS surface BRDF/Albedo retrieval. 1: Algorithm performance. *Journal of Geophysical Research*, *108*(D5), 4158. doi:10.1029/2002JD002803.

Johnson, E. A., & Miyanishi, K. (1997). *Forest fires: Behavior and ecological effects*. San Diego, CA: Academic Press.

Justice, C., Townshend, J., Vermote, E., Masuoka, E., Wolfe, R., Saleous, N., et al. (2002a). An overview of MODIS land data processing and product status. *Remote Sensing of Environment*, *83*, 3–15.

Justice, C. O., Giglio, L., Korontzi, S., Owens, J., Morisette, J., Roy, D. P., et al. (2002b). The MODIS fire products. *Remote Sensing of Environment*, *83*, 244–262.

Justice, C. O., Smith, R., Gill, M., & Csiszar, I. (2003). A review of current space-based fire monitoring in Australia and the GOFC/GOLD program for international coordination. *International Journal of Wildland Fire*, *12*, 247–258.

Kasischke, E. S., & French, N. H. F. (1995). Locating and estimating the areal extent of wildfires in Alaskan boreal forests using multiple-season

AVHRR NDVI composite data. *Remote Sensing of Environment*, *51*, 263–275.

Kaufman, Y. J., Justice, C. O., Flynn, L. P., Kendall, J. D., Prins, E. M., Giglio, L., et al. (1998). Potential global fire monitoring from EOS-MODIS. *Journal of Geophysical Research, [Atmospheres]*, *103*, 32215–32238.

Kaufman, Y. J., & Remer, L. (1994). Detection of forests using mid-IR reflectance: An application for aerosol studies. *IEEE Transactions on Geoscience and Remote Sensing*, *32*, 672–683.

Kimes, D. S. (1983). Dynamics of directional reflectance factor distributions for vegetation canopies. *Applied Optics*, *22*, 1364–1372.

Korontzi, S., Roy, D. P., Justice, C. O., & Ward, D. E. (2004). Modeling and sensitivity analysis of fire emissions in southern African during SAFARI 2000. *Remote Sensing of Environment*, *92*, 255–275.

Korovin, G. N. (1996). Analysis of the distribution of forest fires in Russia. In J. G. Goldammer, & V. V. Furyaev (Eds.), *Fire in ecosystems of boreal Eurasia* (pp. 112–128). Netherlands: Kluwer Academic Publishers.

Leroy, M., & Hautecoeur, O. (1999). Anisotropy-corrected vegetation indexes derived from POLDER ADEOS. *IEEE Transactions on Geoscience and Remote Sensing*, *37*, 1698–1708.

Lucht, W., & Lewis, P. E. (2000). Theoretical noise sensitivity of BRDF and albedo retrieval from the EOS-MODIS and MISR sensors with respect to angular sampling. *International Journal of Remote Sensing*, *21*, 81–98.

Lucht, W., & Roujean, J. -L. (2000). Considerations in the parametric modeling of BRDF and Albedo from multiangular satellite sensor observations. *Remote Sensing Reviews*, *18*, 343–379.

Matson, M., & Dozier, J. (1981). Identification of subresolution high temperature sources using a thermal IR sensor. *Photogrammetric Engineering and Remote Sensing*, *47*, 1311–1318.

Meyer, D., Verstraete, M., & Pinty, B. (1995). The effect of surface anisotropy and viewing geometry on the estimation of NDVI from AVHRR. *Remote Sensing Reviews*, *12*, 3–27.

Miura, T., Huete, A. R., van Leeuwen, W. J. D., & Didan, K. (1998). Vegetation detection through smoke filled AVIRIS images: An assessment using MODIS band passes. *Journal of Geophysical Research*, *103*(D24), 32001–32011.

Morisette, J. T., Giglio, L., Csiszar, I., & Justice, C. O. (in press). Validation of the MODIS active fire product over southern Africa with ASTER data. *International Journal of Remote Sensing*.

Morisette, J. T., Privette, J. L., & Justice, C. O. (2002). A framework for the validation of MODIS land products. *Remote Sensing of Environment*, *83*, 77–96.

Murphy, P. J., Stocks, B. J., & Kasischke, E. S. (1999). Historical fire records in North American boreal forest. In E. S. Kasischke, & B. J. Stocks (Eds.), Fire, climate change and carbon cycling in boreal forest. *Ecological studies series* (pp. 274–288). New York: Springer.

Pereira, J. M. C. (2003). Remote sensing of burned areas in tropical savannas. *International Journal of Wildland Fire*, *12*, 259–270.

Pereira, J. M. C., Chuvieco, E., Beaudoin, A., & Desbois, N. (1997). Remote sensing of burned areas: A review. In E. Chuvieco (Ed.), A review of remote sensing methods for the study of large wildland fires. *Report of the Megafires Project ENV-CT96-0256, August 1997* (pp. 127–183). Alcala de Henares, Spain: Universidad de Alcala.

Pinty, B., & Verstraete, M. (1992). On the design and validation of bidirectional reflectance and albedo models. *Remote Sensing of Environment*, *41*, 155–167.

Prins, E. M., & Menzel, W. P. (1992). Geostationary satellite detection of biomass burning in South America. *International Journal of Remote Sensing*, *13*, 2783–2799.

Rebelo, L., Lewis, P. E., & Roy, D. P. (2004). A temporal-BRDF model-based approach to change detection. *Proceedings of IEEE Geoscience and Remote Sensing Symposium 2004 (IGARSS), September 20–24, 2004*. Alaskan Egan Convention Center: Anchorage.

Robinson, J. M. (1991). Fire from space: Global fire evaluation using infrared remote sensing. *International Journal of Remote Sensing*, *12*(1), 3–24.

Roy, D. P. (2000). The impact of misregistration upon composited wide field of view satellite data and implications for change detection. *IEEE Transactions on Geoscience and Remote Sensing*, *38*, 2017–2032.

Roy, D. P. (2003). SAFARI 2000 July and September MODIS 500 m burned area products for Southern Africa. In Nickeson J., et al., (Eds.), *SAFARI 2000 CD-ROM series*, *vol. 3*. Greenbelt, MD, USA: National Aeronautics and Space Administration, Goddard Space Flight Center.

Roy, D. P., Borak, J., Devadiga, S., Wolfe, R. E., Zheng, M., & Descloitres, J. (2002a). The MODIS land product quality assessment approach. *Remote Sensing of Environment*, *83*, 62–76.

Roy, D. P., Frost, P. G. H., Justice, C. O., Landmann, T., Le Roux, J. L., Gumbo, K., et al. (in press). The Southern Africa Fire Network (SAFNet) regional burned area product validation protocol. *International Journal of Remote Sensing*.

Roy, D. P., Giglio, L., Kendall, J. D., & Justice, C. O. (1999). Multitemporal active-fire based burn scar detection algorithm. *International Journal of Remote Sensing*, *20*, 1031–1038.

Roy, D. P., & Landmann, T. (in press). Characterizing the surface heterogeneity of fire effects using multi-temporal reflective wavelength data. *International Journal of Remote Sensing*.

Roy, D. P., Lewis, P. E., & Justice, C. O. (2002b). Burned area mapping using multi-temporal moderate spatial resolution data—A bi-directional reflectance model-based expectation approach. *Remote Sensing of Environment*, *83*, 263–286.

Russell-Smith, J., Yates, C., Edwards, A., Allan, G. E., Cook, G. D., Cooke, P., et al. (2003). Contemporary fire regimes of northern Australia, 1997–2001: Changes since Aboriginal occupancy, challenges for sustainable management. *International Journal of Wildland Fire*, *12*, 283–297.

Sa, A. C. L., Pereira, J. M. C., Vasconcelos, M. R. P., Silva, J. M. N., Reibeiro, N., & Awasse, A. (2003). Assessing the feasibility of sub-pixel burned area mapping in miombo woodlands of northern Mozamibique using MODIS imagery. *International Journal of Remote Sensing*, *24*, 1783–1796.

Schaaf, C. B., Gao, F., Strahler, A. H., Lucht, W., Li, X., Tsang, T., et al. (2002). First operational BRDF, Albedo and Nadir reflectance products from MODIS. *Remote Sensing of Environment*, *83*, 135–148.

Scholes, M. C., & Andreae, M. O. (2000). Biogenic and pyrogenic emissions from Africa and their impact on global atmosphere. *Ambio*, *29*, 23–29.

Serra, J. (1986). Introduction to mathematical morphology. *Computer Vision, Graphics, and Image Processing*, *35*, 283–305.

Setzer, A. W., & Pereira, M. C. (1991). Amazonia biomass burnings in 1987 and an estimate of their tropospheric emissions. *Ambio*, *20*, 19–22.

Setzer, A. W., Pereira, M. C., & Pereira, A. C. (1992). The use of NOAA satellites in the detection of fires in Brazil. *Climanalise (INPE/Brasil)*, *7*, 41–53.

Shvidenko, A. Z., & Nilsson, S. (2000). Extent, distribution, and ecological role of fire in Russian forests. In E. S. Kasischke, & B. J. Stocks (Eds.), *Fire, climate change, and carbon cycling in the boreal forest* (pp. 132–150). New York: Springer-Verlag New York, Inc.

Simon, M., Plummer, S., Fierens, F., Hoelzemann, J. J., & Arino, O. (2004). Burnt area detection at global scale using ATSR-2: The GLOBSCAR products and their qualification. *Journal of Geophysical Research*, *109*(D14) (D14S0210.1029/2003JD003622).

Stocks, B. J. (1998). Climate change and forest fire potential in Russian and Canadian boreal forest. *Climate Change*, *38*, 1–13.

Stocks, B. J., Cahoon, D. R., Cofer III, J. R., & Levine, J. S. (1996). Monitoring large-scale forest-fire behavior in northeastern Siberia using NOAA-AVHRR satellite imagery. *Biomass Burning and Global Change*, *2*, 802–807.

Stocks, B. J., Goldammer, J. G., Cahoon, D. R., & Frost, P. (2001). Global fire monitoring: International policy requirements. *Forest fire monitor-*

ing and mapping: A component of global observation of forest cover, November 3–5 1999 (pp. 79–84). Ispra, Italy: JRC.

Stronach, N. R. H., & McNaughton, S. J. (1989). Grassland fire dynamics in the Serengeti ecosystem, and a potential method of retrospective estimating fire energy. *Journal of Applied Ecology*, *26*, 1025–1033.

Swap, R. J., Annegarn, H. J., Suttles, J. T., Haywood, J., Helmlinger, M. C., Hely, C., et al. (2002). The Southern African Regional Science Initiative (SAFARI 2000): Overview of the dry-season field campaign. *South African Journal of Science*, *98*, 125–130.

Tansey, K., Grégoire, J. M., Stroppiana, D., Sousa, A., Silva, J., Pereira J. M. C., et al. (2004). Vegetation burning in the year 2000: Global burned area estimates from SPOT VEGETATION data. *Journal of Geophysical Research*, *109*(D14S03). doi:10.1029/2003JD003598.

Tapper, N. J., Garden, G., Gill, J., & Fernon, J. (1993). The climatology and meteorology of high fire danger in the Northern Territory. *Rangeland Journal*, *15*, 339–351.

Townshend, J. R. G., & Justice, C. O. (2002). Towards operational monitoring of terrestrial systems by moderate-resolution remote sensing. *Remote Sensing of Environment*, *83*, 351–359.

UNEP. (2002). *Global Environment Outlook 3*. Earthscan Publications, London, 446, 351–359.

van der Werf, G., Randerson, J. T., Collatz, G. J., & Giglio, L. (2003). Carbon emissions from fires in tropical and subtropical ecosystems. *Global Change Biology*, *9*, 547–562.

Vermote, E. F., El Saleous, N. Z., & Justice, C. O. (2002). Operational atmospheric correction of the MODIS data in the visible to middle infrared: First results. *Remote Sensing of Environment*, *83*, 97–111.

Wanner, W., Strahler, A. H., Hu, B., Lewis, P., Muller, J. -P., Li, X., et al. (1997). Global retrieval of bi-directional reflectance and albedo over land from EOS MODIS and MISR data: Theory and algorithms. *Journal of Geophysical Research*, *102*, 17143–17162.

Whittaker, E., & Robinson, G. (1960). *The calculus of observations*. 4th edition. Glasgow: Blackie & Son Ltd.

Williams, R. J., Griffiths, A. D., & Allan, G. E. (2002). Fire regimes and biodiversity in the wet–dry tropical landscapes of northern Australia. In R. A. Bradstock, J. E. Williams, & A. M. Gill (Eds.), *Flammable Australia: The fire regimes and biodiversity of a continent* (pp. 281–304). Cambridge, UK: Cambridge University Press.

Wolfe, R. E., Nishihama, M., Fleig, A. J., Kuyper, J. A., Roy, D. P., Storey, J. C., et al. (2002). Achieving sub-pixel geolocation accuracy in support of MODIS land science. *Remote Sensing of Environment*, *83*, 31–49.

Wolfe, R. E., Roy, D. P., & Vermote, E. F. (1998). The MODIS land data storage, gridding and compositing methodology: L2 grid. *IEEE Transactions on Geoscience and Remote Sensing*, *36*, 1324–1338.

WWW1, MODIS Land Surface Reflectance User's Guide, http://modis-sr.ltdri.org/html/guide.htm

Zarco-Tejada, P. J., Rueda, C. A., & Ustin, S. L. (2003). Water content estimation in vegetation with MODIS reflectance data and model inversion methods. *Remote Sensing of Environment*, *85*(1), 109–124.

Zhang, Y. -H., Wooster, M. J., Tutubalina, O., & Perry, G. L. W. (2003). Monthly burned area and forest fire carbon emission estimates for the Russian Federation from SPOT VGT. *Remote Sensing of Environment*, *87*, 1–15.